



Quantifying Drivers of Tropospheric OH and Its Trends: Sensitivity to Atmospheric Processes and Implications for Methane Lifetime

Xuewei Hou^{1,2*}, Ryan Hossaini^{1*}, Oliver Wild¹, Andrea Mazzeo¹, Richard J. Pope^{3,4}, Ye Wang¹,
5 Siyuan Wang⁵, Yuanhong Zhao⁶, James Lee^{7,8}, Bin Zhu², Tianliang Zhao², Alok K. Pandey⁹

¹Lancaster Environment Centre, Lancaster University, Lancaster, LA1 4YW, UK.

²Collaborative Innovation Center on Forecast and Evaluation of Meteorological Disasters, School of Atmospheric Physics, Nanjing University of Information Science and Technology, Nanjing, 210044, China.

³School of Earth and Environment, University of Leeds, Leeds, LS2 9JT, UK.

10 ⁴National Centre for Earth Observation, University of Leeds, Leeds, LS2 9JT, UK.

⁵Department of Atmospheric Sciences, University of Miami, Florida, FL 33124, USA.

⁶State Key Laboratory of Physical Oceanography, Ocean University of China, Qingdao, 266100, China.

⁷Department of Chemistry, University of York, York, YO10 5DD, UK.

⁸National Centre for Atmospheric Science, University of York, York, YO10 5DD, UK.

15 ⁹Department of Environmental Sciences, Deshbandhu College, University of Delhi, New Delhi, 110019, India.

Correspondence to: Xuewei Hou (x.hou4@lancaster.ac.uk) and Ryan Hossaini (r.hossaini@lancaster.ac.uk)

Abstract: The hydroxyl radical (OH) is a critical determinant of global oxidative capacity and trace gas lifetimes, but its variation remains poorly constrained. This study investigates the sensitivity of modelled tropospheric OH concentration changes to physical and chemical processes using the FRSGC/UCI chemistry transport model. We show
20 that simulated tropospheric O₃ and NO₂ agree well with satellite observations, but that annual variations in CO do not, likely due to uncertainties in biomass burning emissions in the southern hemisphere and overestimated CO trends over Asia. This discrepancy, along with the background increase in CO, may lead to an underestimation of OH increase or overestimation of OH decrease from 2000 to 2017. Changes in tropospheric OH column show substantial spatial heterogeneity, with increases in OH in high-emission regions and decreases in the tropics. Global mean OH trends are
25 dependent on the assumed trend in emissions: with dynamic emissions there is little change in OH, while under annually invariant emissions, there is a substantial increase in OH due to meteorological conditions alone. Inclusion of water vapor UV absorption, heterogeneous reactions, and updates to the OH + NO₂ reaction rate have a smaller impact on OH trend, but decrease OH levels by 3.6%, 5.8%, and 7.0%, respectively, increasing CH₄ lifetimes by 4.2%, 5.2%, and 8.4%. Incorporating oceanic CH₃CHO emissions reduces global mean OH by up to 1.5%, increasing the CH₄
30 lifetime by up to 1.6%. These results provide a quantitative basis for understanding the drivers of tropospheric OH variability and their implications for global methane chemistry.



1 Introduction

The hydroxyl radical (OH) is one of the most critical reactive species in the troposphere, regarded as the atmosphere's primary cleansing agent due to its role in initiating the oxidation of a wide array of trace gases, including nitrogen oxides (NO_x), methane (CH₄), carbon monoxide (CO), and most volatile organic compounds (VOCs) (Holmes et al., 2013; Turner et al., 2019). The abundance and distribution of OH strongly influences the overall oxidative capacity of the atmosphere, thus affecting the lifetime of species relevant to both air quality and climate (Crutzen, 1973; Lawrence et al., 2001; Naik et al., 2013; Zhao et al., 2019). Understanding the variability in OH and exploring the underpinning drivers is thus of major importance for predicting future atmospheric composition, including the interactions between natural and anthropogenic emissions and climate change (Stevenson et al., 2020; Lelieveld et al., 2016; Chua et al., 2023).

Changes in OH concentrations are driven by a multitude of factors, including variations in precursor emissions, meteorological conditions, and the availability of sunlight and water vapor, all of which affect photochemical reaction rates (Logan et al., 1981; Brasseur and Solomon, 2005). The balance between OH production and loss is governed by a set of interconnected processes, notably ozone (O₃) photolysis, reactions with CH₄ and CO, and regeneration cycles involving NO_x and organic peroxy radicals (RO₂) (Fiore et al., 2024). These complex photochemical processes collectively result in a highly heterogeneous spatial and temporal distribution of OH, with concentrations typically peaking in tropical regions where both solar radiation and water vapor are most abundant (Spivakovsky et al., 2000; Anderson et al., 2024).

An important finding from model intercomparisons is that most chemical transport models (CTMs) and chemistry-climate models (CCMs) underestimate the CH₄ lifetime against OH oxidation in the troposphere (τ_{CH_4}) compared to estimates based on observations. Multi-model mean values of τ_{CH_4} from the Hemispheric Transport of Air Pollution (HTAP), Atmospheric Composition Change: the European Network of Excellence (ACCENT), and Atmospheric Chemistry and Climate Model Intercomparison Project (ACCMIP) model intercomparisons were 10.2 (± 1.7), 9.7 (± 1.7) and 9.7 (± 1.5) years, respectively (Fiore et al., 2009; Shindell et al., 2006; Naik et al., 2013), whereas observationally-constrained estimates, such as those of Prather et al. (2012), suggest a longer τ_{CH_4} of 11.2 (± 1.3) years. This bias in τ_{CH_4} implies that most models overestimate OH concentrations. However, a multitude of processes influence OH concentration, many of which are relatively poorly understood and/or offer limited observational constraint (e.g. Fiore et al., 2024). Detailed sensitivity analysis also reveals that the drivers of OH concentration and its variability can differ substantially across models (Wild et al., 2020) and thus attributing the causes of OH biases is challenging.

In recent years, several new research findings have emerged with potential importance for understanding tropospheric OH and the modelling of its abundance. First, Prather and Zhu (2024) examined the absorption of ultraviolet radiation (UV) by water vapour (H₂O), previously thought to be minor, and its effect on tropospheric photolysis rates. They showed that inclusion of this process in a global CTM reduced OH primary production and increased τ_{CH_4} by ~4%. The study highlighted that water vapour UV absorption may partly resolve some of the apparent low τ_{CH_4} bias present in other models.



Second, while the potential importance of heterogeneous chemistry for tropospheric oxidants is well established from lab studies (e.g. Thornton et al., 2003; Stewart et al., 2004), observations (e.g. Cantrell et al., 1996; Tabazadeh et al., 2004) and modelling work (e.g. Jacob, 2000; Tie et al., 2003; Macintyre and Evans, 2010), recent findings have reaffirmed and extended current understanding. Using the GEOS-Chem CTM with revised uptake coefficients, Holmes et al. (2019) showed that inclusion of heterogeneous NO_x chemistry extended the model estimate of τ_{CH_4} by 6.9% relative to a model run without heterogeneous chemistry. Contrary to some previous findings, they showed that heterogeneous chemistry on clouds exerts an effect of similar magnitude to that occurring on aerosols. Holmes et al. (2019) also emphasized the importance of accounting for entrainment limitations when parameterizing cloud heterogeneous processes, an approach that has yet to be adopted in most models. The effects of heterogeneous chemistry on tropospheric composition have also been examined by Ha et al. (2021) who reported an increase in τ_{CH_4} of 5.9% due to its inclusion in the CHASER MIROC Earth System Model.

Third, more detailed measurements of the rate coefficient for the termolecular OH + NO₂ reaction ($k_{\text{OH}+\text{NO}_2}$) have been reported by Amedro et al. (2019, 2020) and Rolletter et al. (2025). The rate of this reaction exerts a strong influence on the tropospheric abundance of NO_x and OH and is therefore of fundamental importance (e.g. Newsome and Evans, 2017; Christian et al., 2018). The two new studies report that $k_{\text{OH}+\text{NO}_2}$ shows only a weak dependence on water vapor over the tested range of partial pressures. They recommend a rate coefficient of $(1.23 \pm 0.04) \times 10^{-11} \text{ cm}^3 \cdot \text{s}^{-1}$ at 295 K and 1 atm. We compare this with the value of $1.1 \times 10^{-11} \text{ cm}^3 \cdot \text{s}^{-1}$ at 298 K and 1 atm for the OH + NO₂ + M → HONO₂ pathway recommended by the most recent NASA–Jet Propulsion Laboratory (JPL) report (Burkholder et al., 2020), neglecting the role of the alternative HOONO formation pathway which is assumed to reform OH and NO₂.

Fourth, positive sea-to-air fluxes of a range of oxygenated VOCs have been observed in field studies (e.g. Yang et al., 2014; Phillips et al., 2021). While the magnitude and variability of these VOC emissions remain uncertain, in the remote marine boundary layer these species may provide a substantial local OH sink, with oceanic emissions of acetaldehyde (CH₃CHO) postulated as being particularly important (e.g. Read et al., 2012). To date, there have been very few global model assessments of the significance of this effect, but a growing number of studies highlight oceanic CH₃CHO emissions as a contributor to missing OH reactivity and hence a cause of bias in estimates of CH₄ lifetime (e.g. Wang et al., 2019; Travis et al., 2020).

Alongside constraining the processes that lead to OH production and loss, over the past few decades numerous observational and modeling studies have sought to quantify interannual variability and possible long-term trends in OH concentration, both regionally and globally. While direct measurements of OH concentration are challenging due to its short atmospheric lifetime (on the order of seconds), indirect methods such as inverse modeling based on the observed atmospheric burdens of CH₄ and methyl chloroform (MCF) have provided valuable insights (Montzka et al., 2011; Naik et al., 2013; Patra et al., 2021; Prinn et al., 2000; Thompson et al., 2024). In addition, satellite observations combined with steady-state chemical approaches have recently been used to infer mid-tropospheric OH variability, suggesting relatively stable OH over time with O₃ as a primary driver and CO playing a larger role during intense biomass burning years (Pimlott et al., 2022). Although these studies suggest that global mean OH concentration has remained relatively stable, with fluctuations driven by interannual variability in the emissions of OH precursors and sinks such as CO,



VOCs, and NO_x, as well as by meteorological factors (Prinn et al., 2000; Turner et al., 2017), substantial uncertainties persist regarding the temporal trends in regional OH concentration, particularly in the tropics and mid-latitudes (Patra et al., 2014; Anderson et al., 2024). Some studies indicate a decrease in OH from about 2005 (Rigby et al., 2017; McNorton et al., 2016). Other studies have found evidence of increasing OH during 1980–2010 dominated by elevated primary production and reduced loss of OH due to decreasing CO after 2005 (Chua et al., 2023; Stevenson et al., 2020; Zhao et al., 2020). Attributing OH variability remains challenging, with different models showing widely differing responses in OH concentrations to changes in these drivers, particularly to NO_x and humidity (Wild et al., 2020; Nicely et al., 2020). These discrepancies highlight the importance of improving both observational coverage and model representation of OH-related processes in the troposphere.

In this study, we employ a global CTM to (1) examine the response of global and regional OH concentrations to a range of factors, focusing on recent developments including UV absorption by water vapour, heterogeneous chemistry, the $k_{\text{OH}+\text{NO}_2}$ rate coefficient, and CH₃CHO oceanic emissions, and (2) analyze the interannual variability and trends of global and regional OH and quantify their drivers since year 2000. The paper is structured as follows. Section 2 describes the CTM and recent updates, including the addition of heterogeneous chemistry on cloud and aerosol surfaces. It also describes the model sensitivity experiments that were performed and the observational datasets used to evaluate the model. Section 3 provides an evaluation of the CTM, focusing on its ability to reproduce measurements of key gases relevant to the OH budget (e.g. tropospheric O₃, NO_x, CO). Our main results are presented in Section 4, including our model sensitivity analysis of global and regional OH concentrations, OH budgets, impacts of oceanic CH₃CHO emissions, and regional and global OH trends. A summary with concluding remarks is given in Section 5.

2 Model and Methods

2.1 Chemistry Transport Model

The global chemistry transport model (CTM) used here is the Frontier Research System for Global Change version of the University of California, Irvine (FRSGC/UCI CTM) described in Wild and Prather (2000). The model has been widely used to study the chemistry and transport of tropospheric trace gases, including O₃ and OH (Wild et al., 2020), and the results have contributed to model intercomparison studies such as the Hemispheric Transport of Air Pollution (HTAP) project (Fiore et al, 2009). The offline CTM uses meteorological data generated with the European Centre for Medium-Range Weather Forecasts (ECMWF) Integrated Forecasting System (IFS) version Cy38r1. In this work, the model was run at a T42 horizontal resolution (2.8°×2.8°) with 57 vertical levels extending from the surface to 0.1 hPa.

2.2 Gas phase chemistry

The model includes an explicit treatment of HO_x/O_x/NO_x chemistry, CH₄ oxidation, and lumped non-methane hydrocarbon (NMHC) chemistry for the representative species butane, propene, xylene and isoprene (Wild, 2007). The updated version of the CTM used here contains 75 bimolecular reactions, 15 termolecular reactions and 21 photolysis reactions, summarized in **Tables S1 to S3**. Rate constants are principally taken from the most recent JPL evaluation



(Burkholder et al., 2020). A notable exception is for the reaction of OH + NO₂ for which we use the expressions given by Amedro et al. (2019). Recent updates to the model also include a treatment of H₂O ultraviolet absorption following Prather and Zhu (2024).

2.3 Heterogeneous chemistry

140 For this study we have added a treatment of heterogeneous chemistry to the model. This uses a standard reaction probability formulation (e.g. Jacob, 2000) based on prescribed uptake coefficients (γ) for different cloud particles and aerosol surfaces. The first order rate coefficient, k (s⁻¹), for the heterogeneous removal of a species to cloud or aerosol is expressed as:

$$k = 0.25 \times c \times \text{SAD} \times \gamma \quad (1)$$

145 where c is the mean square molecular speed (cm·s⁻¹) and SAD (cm²·cm⁻³) is the available cloud particle or aerosol surface area density. The molecular speed is given by:

$$c = 100 \sqrt{\frac{8RT}{\pi M}} \quad (2)$$

where R is the ideal gas constant (8.315 J·mol⁻¹·K⁻¹), T is temperature (K) and M is the molar mass of the gas (kg·mol⁻¹).

A summary of the heterogeneous reactions included in the CTM is given in **Table S4**. These include the hydrolysis of
150 N₂O₅ to form nitric acid on cloud ice and liquid water droplets and on five aerosol types: sea-salt, dust, sulphate, black carbon and organic carbon. We also include heterogeneous reactions of NO₂, NO₃ and HO₂ on the same sets of surfaces. The adopted γ values for each surface, some of which depend on temperature and relative humidity, are taken from the literature and summarized in **Table S4**.

For cloud ice and liquid water droplets, tropospheric surface area density is calculated online using the ice water content
155 (IWC) and liquid water content (LWC) fields from the ECMWF IFS meteorological data and following the expressions outlined by Holmes et al. (2019).

$$\text{SAD}_{\text{ice}} = \frac{6.75 \times \text{IWC}}{\rho \times r(T)} \quad (3)$$

$$\text{SAD}_{\text{liq}} = \frac{3 \times \text{LWC}}{\rho \times r} \quad (4)$$

In equations (3) and (4) above, ρ denotes the density of ice (916.7 kg·m⁻³) and liquid water (1000 kg·m⁻³), respectively.
160 The effective radius ($r(T)$) for ice particles is calculated as a function of temperature (T) using the empirically-based parameterization of Heymsfield et al. (2014). For liquid water droplets, r is assumed to be 10 μm for marine clouds and 7 μm for continental clouds. When considering the impacts of heterogeneous processes on cloud or ice surfaces, we account for the limitation on uptake due to entrainment of air into clouds under partially cloudy conditions following Holmes et al. (2019), applying the cloud volume fraction from the meteorological fields and assuming a characteristic
165 time scale of one hour.

For aerosols, tropospheric surface area density was calculated from the aerosol climatology described by Bozzo et al.



(2020). This climatology provides monthly mean aerosol mass for five components (sea-salt, dust, sulphate, black carbon and organic carbon) and is based on a reanalysis of atmospheric composition from the Copernicus Atmosphere Monitoring Service (CAM5) over the period 2003-2013. We derived the surface area density for each aerosol type using
170 the particle density, modal radius and size distribution given by Bozzo et al. (2020), accounting for hygroscopic growth governed by the ambient humidity. The resulting annual mean surface area density fields at the surface and in the troposphere are shown in **Figure S1** and **S2**. Note, in this study, the aerosol distributions are prescribed and used only to represent their effects on chemistry and photolysis; aerosol formation and transport are not interactively simulated.

2.4 Emissions

175 In the base run of the model, monthly emissions of CO, NO_x and non-methane volatile organic compounds (NMVOCs) are prescribed largely from CAM5 datasets. Anthropogenic emissions are from version 6.2 of the CAM5-GLOB-ANT inventory (Soulie et al., 2024), aircraft emissions from version 2.1 of CAM5-GLOB-AIR (Granier et al., 2019), biogenic emissions from version 3.1 of CAM5-GLOB-BIO (Sindelarova et al., 2022) and soil NO_x emissions from version 2.4 of CAM5-GLOB-SOI (Simpson and Darras, 2021). Fire emissions are taken from the Global Fire Emissions
180 Database, Version 4.1 (GFED4s) inventory (van der Werf et al., 2017). All emissions vary annually over our full simulation period. Ocean emissions of CO and selected hydrocarbons are taken from the POET emission inventory and are assumed to be climatological (Granier et al., 2005). Lightning NO_x emissions are calculated interactively in the model and vary annually, providing a source of ~5 Tg[N] yr⁻¹.

For each emitted tracer, annual global total emissions over our study period (2000 to 2017) are shown in Figure S3. For
185 CH₄, an annual and latitudinally varying mixing ratio is prescribed using the historical forcing data prepared for CMIP6 from 2000 until 2014 (Meinshausen et al., 2017). After 2014, to match the observed record, the fields are scaled by a globally uniform factor derived from CH₄ measurements from the National Oceanic and Atmospheric Administration (NOAA) global monitoring network.

2.5 Model runs

190 A total of nine model hindcast runs were conducted. Seven of these were long-term runs spanning the period 2000–2017, and two were shorter sensitivity runs covering 2016–2017 only. All runs included a spin-up over the preceding 20-month period. The control run (CTL) included all the processes detailed above. Sensitivity runs were then performed to quantify the OH response to different processes. These include a run with fixed emissions from the year 2000 (fixEmis), a run without UV water vapor absorption (noWVA), a run without heterogeneous chemistry on cloud surfaces
195 (noCloud), a run without heterogeneous chemistry on aerosol surfaces (noAero), a run without heterogeneous chemistry on both cloud and aerosol surfaces (noHete), a run with $k_{\text{OH}+\text{NO}_2}$ taken from the most recent JPL evaluation (JPL) and two shorter runs (ALD-cesm and ALD-geoc) that included oceanic emissions of CH₃CHO. A summary of model runs is provided in **Table 1**.

In the subsequent sections, differences between each sensitivity run and the control are used to quantify the response of
200 global mean OH concentration and τ_{CH_4} to the respective process. We also examine how these factors influence the



temporal trends in OH. Run fixEmis is designed to isolate the effect of meteorological variability on OH. Heterogeneous reactions occurring on cloud and aerosol surfaces may compete for the same species (Holmes et al., 2019), and therefore sensitivity runs were designed to isolate the effects of clouds and aerosols separately, and also to examine their combined impact. Run JPL is used for quantifying the impacts of the updated rate constant for the key OH+NO₂ reaction (Amedro et al., 2019, 2020) on OH and to compare with previous studies (Burkholder et al., 2020).

Our control run included CH₃CHO emissions from biogenic (15.5 Tg·yr⁻¹), biomass burning (2.9 Tg·yr⁻¹), and anthropogenic (9.3 Tg·yr⁻¹) sources only. Runs ALD-cesm and ALD-geoc were identical to the control run except that they additionally included a prescribed monthly ocean CH₃CHO source. These were obtained from models incorporating online parameterizations of the sea-air flux of CH₃CHO. Run ALD-cesm used CH₃CHO emissions for the year 2015 obtained from the Community Earth System Model, version 2.2.0 (CESM2, Emmons et al., 2020), while run ALD-geoc took CH₃CHO emissions from a GEOS-Chem simulation (version 13.4), run with settings similar to Millet et al. (2010) and Wang et al. (2019), respectively. The global annual CH₃CHO ocean sources are 40.8 Tg·yr⁻¹ from CESM2 and 62.7 Tg·yr⁻¹ from GEOS-Chem. The distributions of CH₃CHO ocean emission are shown in Figure S4.

Table 1. Summary of model experiments and settings

Case	Emissions	Water Vapor	Aerosol	Cloud	Aerosol	$k_{\text{OH}+\text{NO}_2+\text{M}}$ at 298K	CH ₃ CHO ocean emissions	Simulation period
CTL	CAMS	on	on	on	on	1.26×10^{-11}	0.0	2000-2017
fixEmis	CAMS_2000	on	on	on	on	1.26×10^{-11}	0.0	2000-2017
noWVA	CAMS	off	on	on	on	1.26×10^{-11}	0.0	2000-2017
noCloud	CAMS	on	off	on	on	1.26×10^{-11}	0.0	2000-2017
noAero	CAMS	on	on	off	on	1.26×10^{-11}	0.0	2000-2017
noHete	CAMS	on	off	off	on	1.26×10^{-11}	0.0	2000-2017
JPL	CAMS	on	on	on	on	1.05×10^{-11}	0.0	2000-2017
ALD-cesm	CAMS	on	on	on	on	1.26×10^{-11}	40.8 Tg·yr⁻¹	2016-2017
ALD-geoc	CAMS	on	on	on	on	1.26×10^{-11}	62.7 Tg·yr⁻¹	2016-2017

Notes: CAMS_2000 indicates that all emissions and prescribed CH₄ are fixed to year 2000 levels, but meteorology varies annually. Cloud refers to the heterogeneous chemistry of N₂O₅, NO₂, NO₃, and HO₂ on cloud surfaces (cloud water droplet, cloud ice). Aerosol refers to the heterogeneous chemistry of N₂O₅, NO₂, NO₃, and HO₂ on five aerosol surfaces (sea salt, dust, black carbon, organic carbon, and sulfate). The reaction coefficient of OH+NO₂ at 298 K ($k_{\text{OH}+\text{NO}_2+\text{M}}$, cm³·molecule⁻¹·s⁻¹) is calculated based on the equations in Table S2. Run JPL used the rate constant from Burkholder et al. (2020).

2.6 Satellite data

As part of our model evaluation, we consider tropospheric column O₃ data from the Aura Ozone Monitoring Instrument/Microwave Limb Sounder (OMI/MLS) dataset over the period 2005–2017. The resolution of the dataset is 1°×1.25° with a latitude range of 59.5°S to 59.5°N and longitude range of 180°W to 180°E. Further details of the OMI/MLS product are discussed by Ziemke et al. (2006).

We use tropospheric NO₂ column from OMI QA4ECV version 1.1 for 2005–2017 released by the Tropospheric



Emission Monitoring Internet Service. The OMI QA4ECV NO₂ data set is based on revised spectral fitting features accounting for improved absorption cross sections, instrument calibration, and surface effects (Boersma et al., 2018; Zara et al., 2018). The data are processed according to the data quality recommendations and were validated against
230 ground measurements (Compernelle et al., 2020). This product includes averaging kernel (AKs) information which has been used for model-satellite comparison to account for the satellite vertical sensitivity (i.e. like-for-like comparisons). To reduce comparison representation errors, each satellite retrieval is spatiotemporally co-located (within 1-hour temporally and the neighboring grid box spatially) with the model and the simulated profile interpolated onto the satellite pressure grid. The model sub-columns are calculated and the AKs applied (as discussed by Archibald et al.
235 (2020)), which are totaled between the surface and tropopause to derive the AK-modified model tropospheric column. Here, each satellite retrieval has been filtered for a cloud radiance fraction <0.5, a quality flag = 1.0, solar zenith angle (SZA) < 80.0°, snow-ice flag < 10.0, tropospheric column NO₂ > -1.0×10¹⁵ molecules/cm² and a AMF_{trop}/AMF_{geo} (geometric AMF) ratio > 0.2.

MOPITT derived CO (Near and Thermal Infrared Radiances) V9 from the NASA Earth data archive are used for 2001–
240 2017. The V9 product provides substantially improved retrieval coverage over land (30–40 % higher than V8) owing to an enhanced cloud detection algorithm and improved calibration of the near-infrared channels, while maintaining retrieval biases generally within ±5 % (Deeter et al., 2022). Individual MOPITT CO retrievals are filtered for a degree of freedom of signal (DOFS) > 1.0. MOPITT CO data has already been pre-filtered for cloud cover in the data product. For the model-satellite comparisons, like for tropospheric column NO₂, the model is spatiotemporally co-located with
245 the retrievals and the model CO profile interpolated onto the satellite pressure grid. The AKs are applied following the approach documented in Archibald et al. (2020) yielding a modified model profile (in vmr). The model sub-columns are then derived and totaled up from the surface to the top-of-atmosphere to calculate the total column.

2.7 Site and vertical profile data

Surface O₃ observations used for model evaluation were obtained from the gridded Tropospheric Ozone Assessment
250 Report (TOAR) global database (Schultz et al., 2017). The TOAR database compiles surface O₃ measurements from thousands of monitoring stations worldwide and provides harmonized metrics derived from quality-controlled observations. We use gridded ozone metrics generated by aggregating station observations within 5° × 5° grid cells for the period 1990–2014. The dataset provides monthly statistical metrics, including daytime mean, nighttime mean, median, and mean rural O₃ concentrations. In this study, the monthly mean O₃ dataset was used for the period 2000–
255 2014 to evaluate the simulated surface O₃ concentrations.

Table 2. Summary of ATom measurements used to evaluate the model simulation

Mission	Month/Year	Total number of observed samples
ATom-1	Jul-Aug 2016	1051 (OH), 1138 (HO ₂), 1270 (CH ₃ CHO)
ATom-2	Jan-Feb 2017	1396 (OH), 1582 (HO ₂), 1315 (CH ₃ CHO)
ATom-3	Sep-Oct 2017	1368 (OH), 1474 (HO ₂), 1497 (CH ₃ CHO)
ATom-4	Apr-May 2018	1233 (OH), 1352 (HO ₂), 1724 (CH ₃ CHO)

Observed vertical profiles of OH and HO₂ obtained during the Atmospheric Tomography Mission (ATom) have been



used to help evaluate the model. The ATom mission consisted of four aircraft campaigns (**Table 2**) with an overarching goal of advancing scientific understanding of the impact of human activities on the tropospheric budget of a wide range of trace gases related to air quality and climate (e.g. Thompson et al., 2022). Measurements were made onboard the NASA DC-8 aircraft in each of the four seasons over a 3-year period (2016–2018), across a large latitude range (~80° N to ~80° S), and up to an altitude of ~12 km (Wofsy et al., 2021). For OH and HO₂, measurements were made using the Airborne Tropospheric Hydrogen Oxides Sensor instrument. For CH₃CHO, measurements were made using the Trace Organic Gas Analyzer instrument. These observational datasets underwent careful calibration and quality assurance prior to public release and have been widely used for atmospheric chemistry research and model evaluation (Duan et al., 2024). The time resolution of these data is 10 seconds for OH and HO₂, and 20 seconds for CH₃CHO. The number of valid measurements is listed in **Table 2**. For comparison to this measurement data, hourly output from the model was sampled along the aircraft flight tracks.

2.8 Trend analysis

Long-term trends in atmospheric trace gas columns, including tropospheric O₃, tropospheric NO₂, total CO column, and tropospheric OH, were estimated using the Theil–Sen slope estimator, a robust non-parametric method that calculates the median of all pairwise slopes (Theil, 1950; Sen, 1968). The statistical significance of trends was assessed with the Mann–Kendall test, a non-parametric method for detecting monotonic trends in time series without assuming a specific data distribution (Mann, 1945; Kendall, 1975). Trend analyses were performed at each grid point for all species. In addition, the global tropospheric mean OH concentration, weighted by mass, was analyzed for seasonal trends to assess temporal variations throughout the year. These methods are particularly suitable for atmospheric chemistry observations and model outputs, which often contain noise, outliers, and non-normally distributed values. Trends in this study were considered significant at the 95 % confidence level ($p < 0.05$).

3 Evaluation

3.1 Satellite data

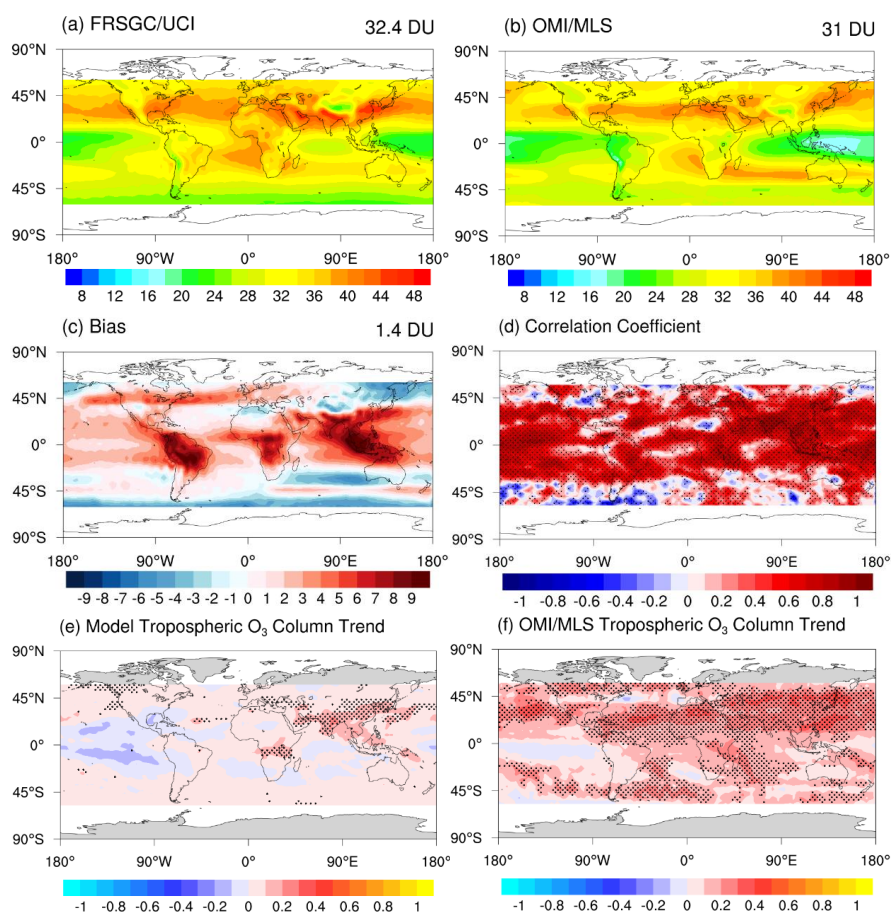
Primary production of tropospheric OH occurs via the photodissociation of tropospheric O₃ by UV radiation ($\lambda < 310$ nm) to produce excited singlet oxygen atoms (O(¹D)) (Talukdar et al., 1998) which may then react with water vapor. Therefore, the ability of models to simulate tropospheric O₃ is of direct importance to accurate simulation of OH.

As shown in **Figure 1 (a-c)**, the model captures the salient features of the spatial distribution of tropospheric O₃ column from OMI/MLS satellite observation well. There is high bias in low latitude regions which may be attributed to the low vertical resolution, difficulty in diagnosing the tropopause and overestimation of the effects of lightning NO_x in the model (Griffiths et al., 2021), and the uncertainties in vertical sensitivity of the observation instrument. The correlation coefficient of the annual mean tropospheric O₃ column between model and observation exceeds 0.6 in most regions and is significant at the 95 % level (**Figure 1d**), suggesting that the year-to-year variations in the simulated and observed tropospheric O₃ column are largely consistent. Exceptions occur in small regions of North America and Northern Africa,



where the correlation coefficient becomes negative. Examination of the corresponding time series indicates that these regions exhibit relatively weak interannual variability in tropospheric O₃, and the year-to-year fluctuations are dominated by a small number of episodic events that are not consistently reproduced by the model. As a result, the correlation metric can turn negative even when the mean seasonal cycle is reasonably captured. This suggests that the poor correlation in these regions is related to low signal-to-noise ratio and episodic variability rather than systematic model bias.

295



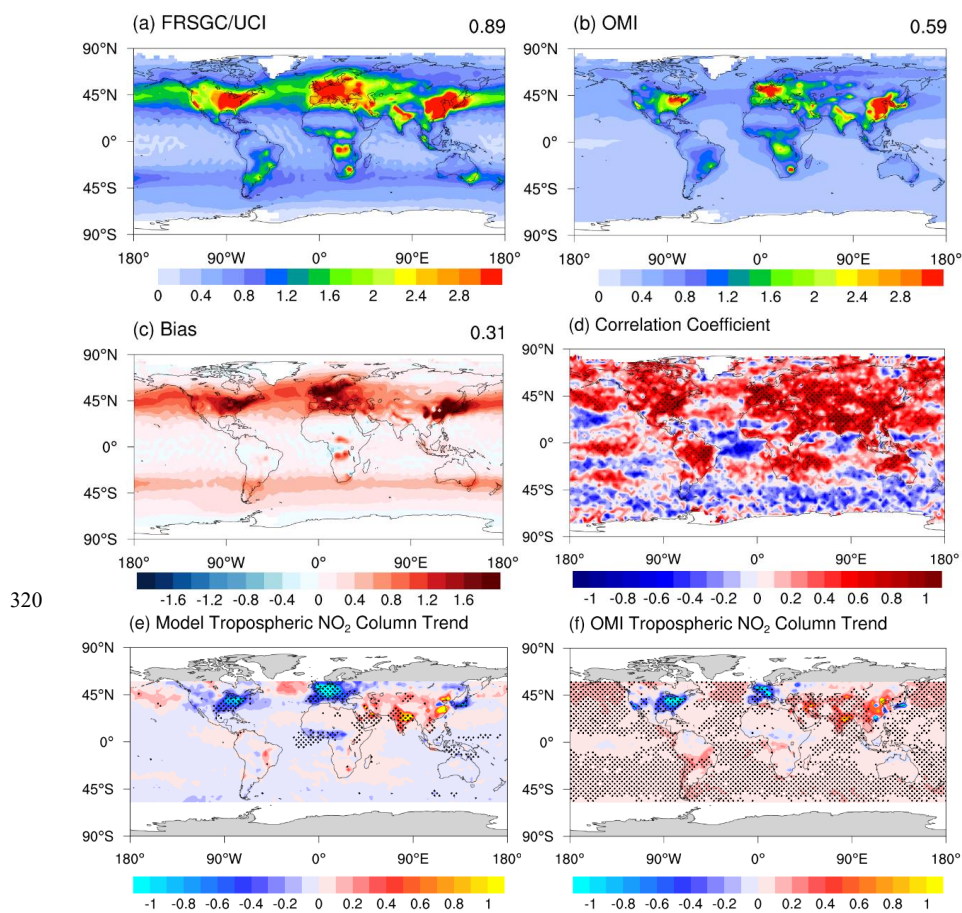
300 **Figure 1. Multiyear average (2005–2017) tropospheric O₃ column (DU) from (a) the model control run and (b) OMI/MLS satellite observations. Panel (c) shows the corresponding mean bias of the tropospheric O₃ column (model minus observation), and (d) shows the correlation coefficient of annual mean tropospheric O₃ column between model and observations. Annual mean tropospheric O₃ column trends (DU·yr⁻¹) are shown in (e) for the model and (f) for satellite observations over the 2005–2017 period. Global mean columns between 60°S–60°N are indicated in the upper right corner of panels (a)–(c). Shaded areas in (d) indicate regions where the correlation is statistically significant at the 95% confidence level (p < 0.05). Trends in panels (e) and (f) were calculated using the Theil–Sen method, and stippling indicates areas with significant trends at the 95% confidence level according to the Mann–Kendall test.**

305

Both the model and observations show significant increase in tropospheric O₃ column from 2000 to 2017, especially over northern hemisphere mid-latitude regions including South and East Asia. Stronger and more significant increases



310 are apparent in the observations (**Figure 1f**). As discussed in previous research, the increase of tropospheric O₃ column is mainly attributed to changes in emissions of O₃ precursors, especially over high pollution regions (Hou et al., 2023; Wang et al., 2022; Ziemke et al., 2019; Young et al., 2018). Over the tropical Pacific Ocean, both the model and observations show decreases in O₃ column. Over southern North America and Mexico, in contrast to the observed +0.2 DU/yr increase, the model shows a weak decrease (**Figure 1e**), which is likely driven by decreases in anthropogenic emissions in the model (Liu et al., 2022). The tropospheric O₃ burdens and budgets align well with previous studies and fall within the reported uncertainty ranges which are listed in **Table S5**. Overall, our simulated results represent the distributions and interannual variations of O₃ well, especially the significant increase over East Asia and decrease over the tropical Pacific Ocean.



320

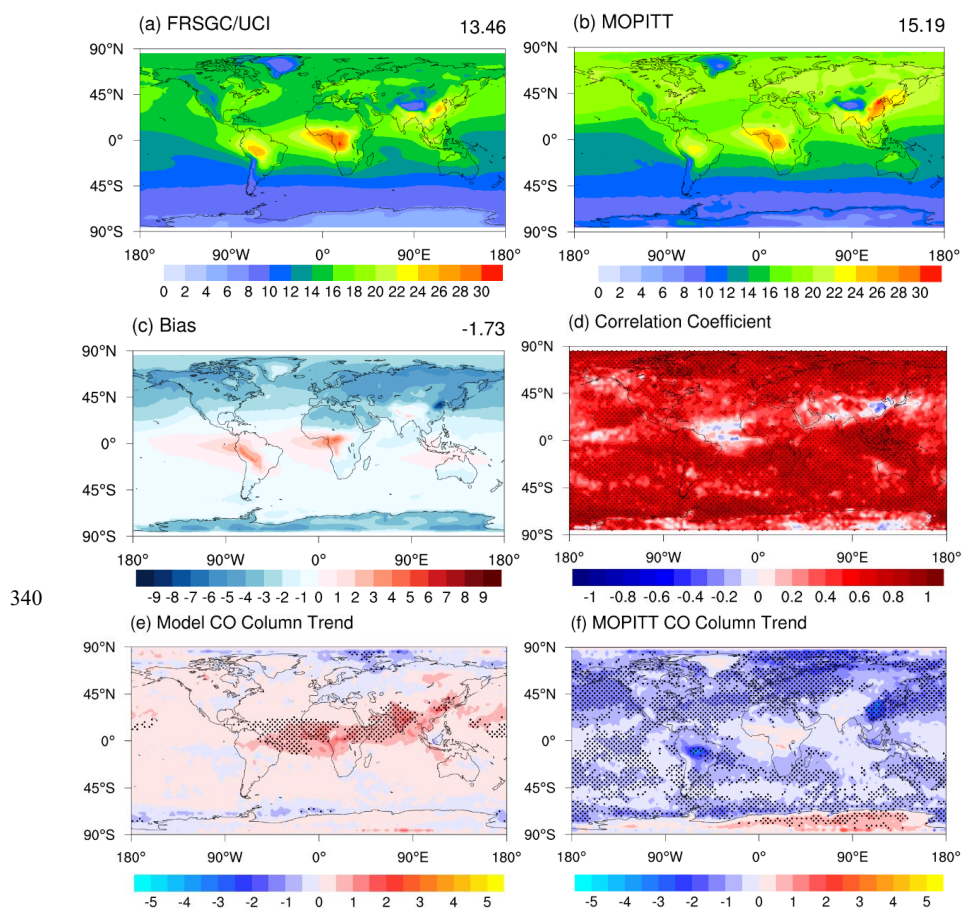
Figure 2. Same as Figure 1, but for tropospheric NO₂ column (10^{15} molecules·cm⁻²) and annual mean tropospheric NO₂ column trends (10^{14} molecules·cm⁻²·yr⁻¹).

As a key precursor of tropospheric O₃ and OH, NO_x has a substantial impact on their distribution and trends. Trends in NO_x may drive the modelled increase in OH (Chua et al., 2023), so it is important to explore how well the modelled NO_x trends match observations. As shown in **Figure 2 (a-d)**, the spatial distribution of tropospheric NO₂ column is simulated well by the model. There is a relatively high model bias in NH mid latitude regions around 45°N, although

325



the satellite data has a relatively large uncertainty here. This positive bias is comparable to that reported in previous
 330 model studies over (e.g. Archibald et al., (2020) in the Northern Hemisphere and Monks et al., (2017) over Europe),
 suggesting that the magnitude of the bias is broadly consistent with current-generation chemistry-climate and
 chemistry-transport models. The simulated interannual variations over our study period match the satellite observations
 well ($R > 0.6$, $p_value < 0.05$), over most of the world, including East Asia, Europe, North America and South Africa.
 While the model performance is weaker in remote regions, the key result is over urban regions with high NO_2 loading
 which will have more influence on OH. The modelled trend in tropospheric NO_2 column is broadly consistent with
 335 previous studies (Elshorbany et al., 2024; Jiang et al., 2022) showing a significant increase over South Asia and most
 parts of East Asia, and a significant decrease over Europe and North America from 2000 to 2017 (**Figure 2e-f**). These
 changes are primarily attributed to variations in emissions (Miyazaki et al., 2017) and match the spatial distribution
 observed in OMI NO_2 data.



340

Figure 3. Same as Figure 1, but for total CO column (10^{17} molecules cm^{-2}) and annual mean total CO column trends (10^{16} molecules $\text{cm}^{-2} \cdot \text{yr}^{-1}$).

Figure 3 (a, b) compares the modelled CO column distribution to that observed from MOPITT. The agreement
 345 between the two datasets is generally strong, although the model underestimates CO in most regions (**Figure 3c**). As



seen in **Figure 3(d)**, the model captures the interannual variations well over most parts of the world ($R>0.6$). The MOPITT CO column generally shows significant decreases across much of the globe, consistent with earlier results from, for example, Yin et al. (2015) and Chua et al. (2023). However, in contrast the modelled CO columns show significant increases over China, India, and Africa with weaker decreases in parts of Europe, North America, and the Middle East (**Figure 3e**). The MOPITT and modelled changes in the CO column show poor agreement, with the model failing to capture the observed decrease reported by MOPITT, particularly over China, India and much of the Southern Hemisphere (SH). A similar mismatch was identified in the modelling study of Chua et al. (2023) which used the Geophysical Fluid Dynamics Laboratory (GFDL) CCM driven by the CMIP6 emission inventory. Chua et al. (2023) note that the mismatch could point towards deficiencies in the emissions that drive the high bias in CO column trends over China and South Asia and in turn lead to the general high bias globally due to transport from these regions, especially via the prevailing westerlies (Zheng et al., 2018). Consistent with this, Gaubert et al. (2020) showed that correcting anthropogenic CO emission in East Asia reduces model bias by 29 % for CO, 11 % for HO₂, and 27 % for OH. In the Southern Hemisphere, the mismatch may partly arise from uncertainties in the biomass burning emission inventory used in the model (Chua et al., 2023). As the main sink of OH in the troposphere, the mismatch and positive trend in CO may lead to underestimation of any OH increase or overestimation of any OH decrease over the 2000–2017 period. Discrepancies in the CO changes may thus have a substantial impact on the modelled interannual variation in OH.

3.2 Surface data

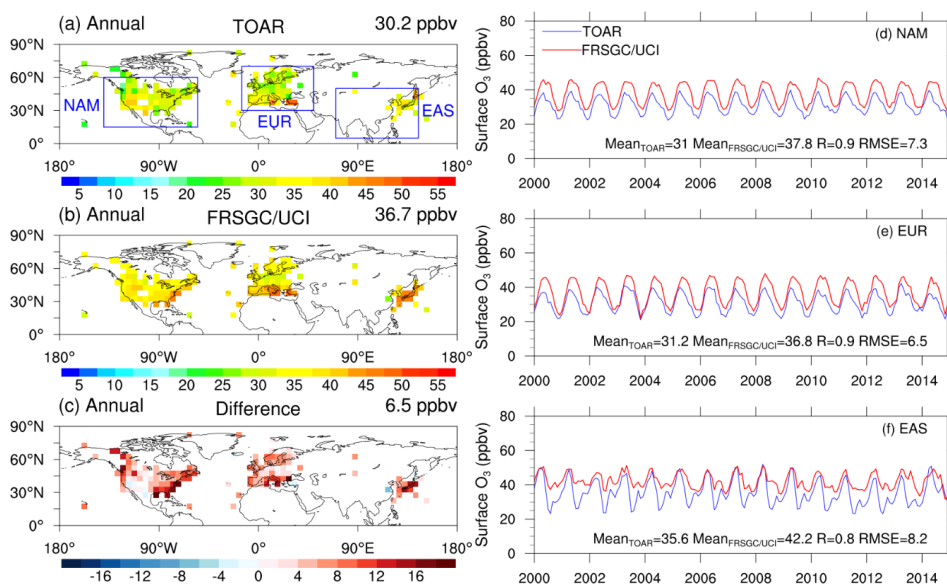


Figure 4. Observed monthly mean surface O₃ (ppbv) from TOAR and corresponding simulated O₃ from the model control run for the period January 2000 to December 2014. Panels (a) and (b) show the distributions of annual mean observed and simulated O₃, respectively, while panel (c) shows the model–observation difference. Panels (d–f) show the corresponding regional mean time series over North America, Europe, and East Asia, respectively, with line colours indicating observations



370 **and model simulations. All modelled means are calculated only for grid squares with available observations. Global mean values are shown in the upper right corner of panels (a–c). The regional mean values, correlation coefficient (R) between observed and simulated regional means, and root mean square error (RMSE) are shown in the lower right corner of panels (d–f).**

375 Simulated monthly mean surface O₃ concentrations for 2000–2014 were evaluated against gridded observations from the TOAR dataset in the northern hemisphere (**Figure 4**). The model reproduces the large-scale spatial distribution and seasonal cycle of surface O₃ well, with enhanced concentrations over major mid-latitude regions such as North America, Europe, and East Asia. However, surface O₃ is generally overestimated in most regions. As an annual global mean, the model simulates 36.7 ppbv compared with 30.2 ppbv from TOAR, corresponding to a positive bias of about 6.5 ppbv. The bias is smaller in January (4.8 ppbv) but increases in July (9.9 ppbv), indicating stronger overestimation during summer when photochemical production is more active. One contribution to this bias is from the relatively coarse
380 vertical resolution of the model, where the 100-m depth of the lowest layer does not fully represent O₃ at the surface, where there may be substantial removal by dry deposition. Despite this bias, the model captures the main spatial patterns and seasonal variability of surface O₃. Regional scatter plots (**Figure S5**) further show that the model captures the observed variability of surface O₃ reasonably well, with correlation coefficients of 0.6–0.8 across North America, Europe, and East Asia, with the strongest agreement over Europe. Evaluation shows comparable performance to the
385 MOZART-4 simulation by Fei et al. (2021) and the CESM FCSD simulation in Hou et al. (2023).

3.3 Vertical profiles of OH and HO₂

The ATom campaign (Wofsy et al., 2021) provides an unprecedented opportunity to test model performance in the remote atmosphere with a detailed suite of chemical observations. **Figure 5** shows modeled OH sampled along the flight tracks and compared to observed OH for ATom-1 (boreal summer 2016), ATom-2 (boreal winter 2017), ATom-3
390 (boreal autumn 2017), and ATom-4 (boreal spring 2018) in each hemisphere from the lowest sampled altitude (~1000 hPa) to 150 hPa.

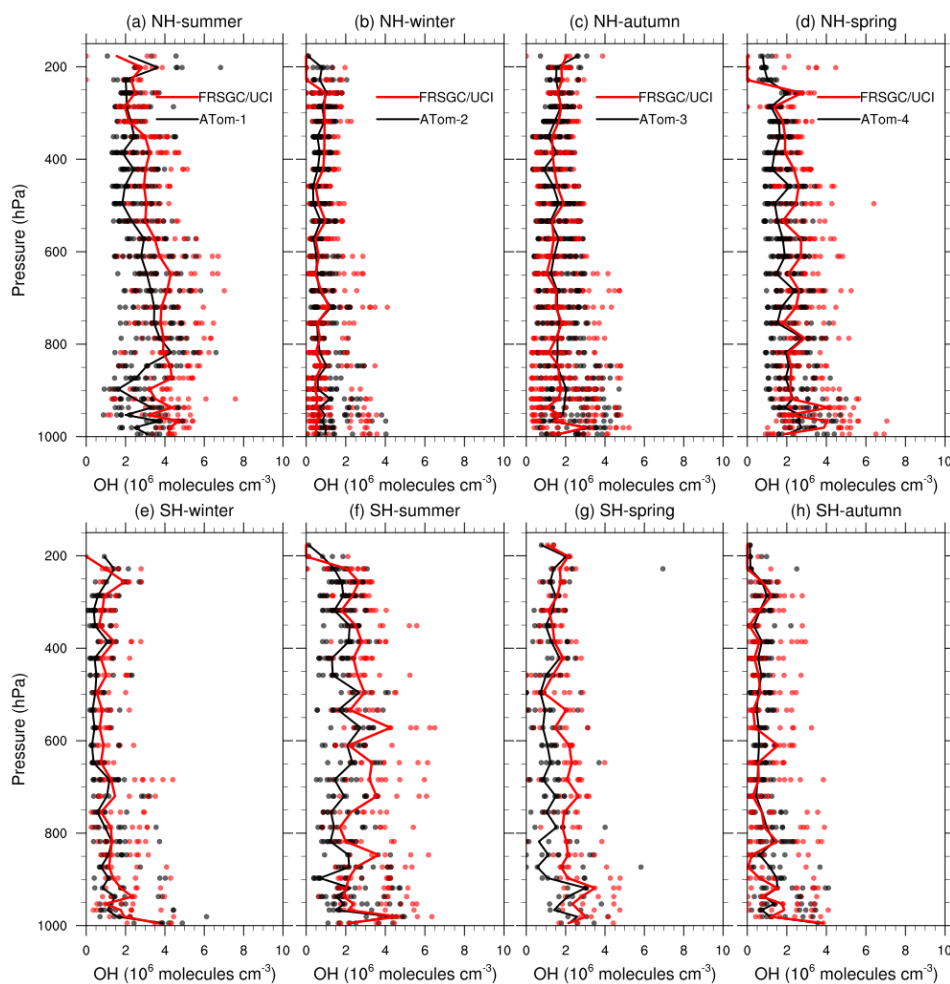


Figure 5. Median OH concentrations (10^6 molecules cm^{-3}) for the Northern Hemisphere (NH, top row) and Southern Hemisphere (SH, bottom) measured during the ATom aircraft missions (black) along with the corresponding results from the model control run (FRSGC/UCl, red). Dashed lines show the observed 25th–75th percentiles.

The model generally reproduces tropospheric OH well, with simulated concentrations falling within observational uncertainty across the environments considered here and no clear systematic bias throughout the troposphere. The model overestimates OH in the northern hemisphere in summer and this may reflect excessive OH production (see previous discussion of O_3 biases and **Figure 1c**) or an underestimated sink from CO (**Figure 3c**). Models tend to overestimate OH on a global scale against constraints from methane and methyl chloroform observations (Shindell et al., 2006; Naik et al., 2013; Nicely et al., 2017), but we find that tropospheric OH is simulated relatively well, within observational uncertainty, in the environments considered here. This good agreement is consistent with box model studies comparing OH with measurements during NASA’s Pacific Exploratory Mission–Tropics (PEM-Tropic B) campaign in the clean remote Pacific (Tan et al., 2001) and a similar analysis by Travis et al. (2020) for ATom 1-2 and Brune et al. (2020) for ATom 1-4.

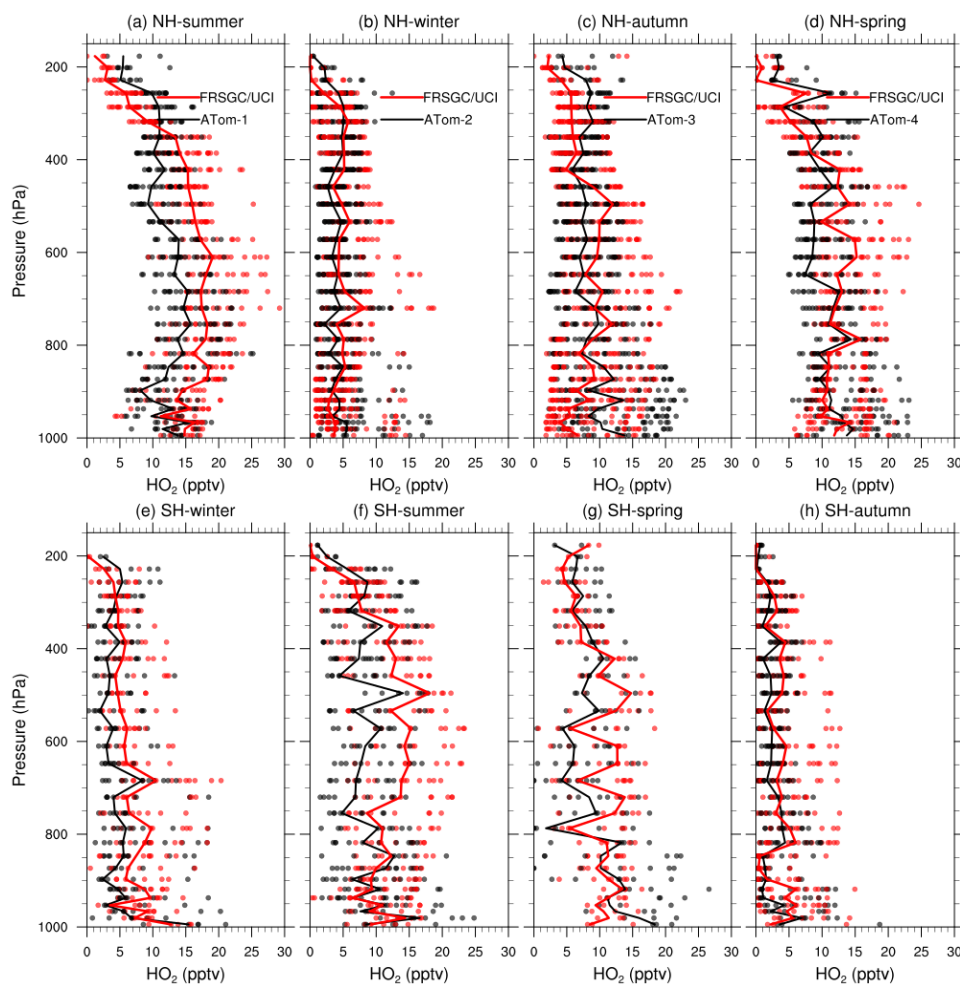


Figure 6. As Figure 5, but for HO₂ (pptv)

Modelled HO₂ is overestimated in the mid-troposphere, except in northern hemisphere winter (**Figure 6**). One possible reason is the influence of biomass-burning emissions. Observations from ATom indicate that air masses influenced by biomass burning, identified using tracers such as HCN and enhanced CO, are frequently encountered in the tropical and subtropical troposphere and can be transported over remote oceans at altitudes of ~1–4 km (e.g. Wofsy et al., 2021; Strode et al., 2018). These air masses contain elevated CO and VOCs that can enhance HO_x cycling and promote HO₂ formation (e.g. Tan et al., 2001; Brune et al., 2020; Fiore et al., 2024), especially in spring and summer. An overestimate in biomass-burning emissions could lead to excessive HO₂ production. However, uncertainties in long-range transport and radical recycling may also contribute to the simulated bias. Overall, the general spatial and temporal variations in HO₂ are represented relatively well, although there is an overestimation remaining in the mid troposphere. For both the OH and HO₂ model-measurement comparisons, the measurement uncertainty of ±35% for each species should be borne in mind (Brune et al., 2020).



4 Results and Discussions

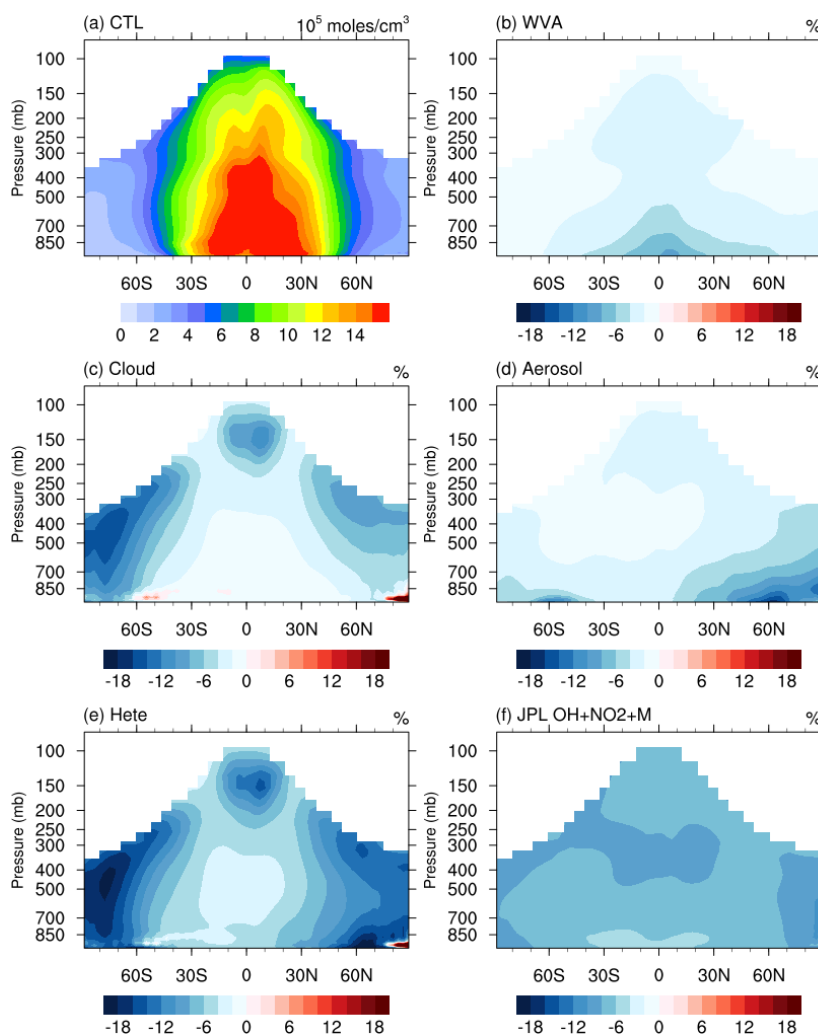
420 4.1 Global tropospheric OH

Global tropospheric mean airmass-weighted OH concentration ($[\text{OH}]_{\text{gm}}$) was calculated for each model run for the year 2000 and as an average for the period 2000-2017 (**Table 3**). For 2000, $[\text{OH}]_{\text{gm}}$ from the control run (10.9×10^5 molecules $\cdot\text{cm}^{-3}$) is very similar to the ACCMIP multi-model mean (± 1 s.d.) estimate of $11.1 (\pm 1.6) \times 10^5$ molecules $\cdot\text{cm}^{-3}$ for the same year (Naik et al. 2013), about 1.8 % lower but well within the full spread of ACCMIP models. The corresponding CH_4 lifetime against tropospheric OH oxidation (τ_{CH_4}) is 10.0 years. For comparison, the multi-model mean estimate from ACCMIP for the same year is 9.7 (± 1.5) years. Our τ_{CH_4} estimate is close to, and within the uncertainty range, of observationally derived estimates, including the 10.2 (9.5-11.1) years estimated by Prinn et al. (2005) and 11.2 (± 1.3) years estimated by Prather et al. (2012). As OH is the principal tropospheric sink of CH_4 , these comparisons suggest that our CTM produces a reasonable simulation of $[\text{OH}]_{\text{gm}}$.

430 **Table 3. Modelled global tropospheric airmass-weighted OH concentration ($[\text{OH}]_{\text{gm}}$) and CH_4 lifetime against tropospheric OH (τ_{CH_4}). Results are shown for the year 2000 and the mean of the period 2000 to 2017.**

	$[\text{OH}]_{\text{gm}}$ (10^5 molec $\cdot\text{cm}^{-3}$)		τ_{CH_4} (years)	
	2000	2000-2017	2000	2000-2017
CTL	10.86	10.87	10.0	9.93
fixEmis	10.88	11.05	10.0	9.77
noWVA	11.24	11.27	9.61	9.52
noCloud	11.12	11.13	9.84	9.76
noAero	11.21	11.22	9.66	9.59
noHete	11.49	11.50	9.49	9.41
JPL	11.62	11.63	9.38	9.31

Figure 7a shows zonal mean OH concentration from the control run averaged over the period 2000-2017. The other panels show percentage differences associated with the selected sensitivity experiments. The control run shows high OH concentrations between 30°S and 30°N in the lower to middle troposphere, with larger values in the northern hemisphere, that reflect the sources of OH, matching the results of previous assessments (Stevenson et al., 2020). Excluding the effects of water vapour UV absorption leads to higher OH throughout the troposphere, especially in the tropical lower troposphere where humidity is relatively high. Water vapor absorption reduces photolysis rates in the troposphere leading to decreases in OH of 6-10% at the surface in the tropics (**Figure 7b**). On a global basis, $[\text{OH}]_{\text{gm}}$ is reduced by 3.6% compared to the control run and τ_{CH_4} is lengthened by ~4.2% (**Table 3**). The magnitude of these responses is in close agreement with that reported by Prather and Zhu (2024).



445 **Figure 7. (a) Zonal mean (latitude-pressure) cross sections of annual mean OH concentration ($10^5 \text{ molec}\cdot\text{cm}^{-3}$) in CTL run and difference in OH (in %) in the troposphere due to (b) removing water vapor UV absorption (WVA), (c) removing cloud heterogeneous reactions (Cloud), (d) removing aerosol heterogeneous reactions (Aerosol), (e) removing all heterogeneous reaction (Hete), and (f) altering the reaction rate for OH+NO₂ (JPL). The troposphere was defined as the region below a climatological tropopause ($p = 300 - 215(\cos(\text{lat}))^2$) following Lawrence et al. (2001).**

The effects of heterogeneous chemistry on cloud surfaces (liquid water and ice) and aerosol are shown in **Figure 7c-e**. The cloud impact peaks at high latitudes in the free troposphere (>10%), while the aerosol impact peaks at mid-latitudes close to the surface. Their combined effect on OH is spatially extensive. The spatial pattern is primarily driven by the vertical distribution of clouds and the near-surface high concentration of aerosol. The differences in their impact stems from differences in where NO_x is removed: aerosols primarily scavenge NO_x in the lower troposphere over industrial regions where NO_x concentrations are high, whereas clouds exert a stronger influence in remote, high-altitude regions where NO_x levels are low (Holmes et al., 2019). As a result, heterogeneous chemistry on cloud surfaces has a



disproportionately large effect on global OH despite occurring in areas with lower NO_x . As shown in **Table 3**, if cloud
455 heterogeneous reactions are neglected, $[\text{OH}]_{\text{gm}}$ increases 2.4%, which results in a 1.7% decrease in the CH_4 lifetime.
Neglecting heterogeneous aerosol reactions yields larger changes: a 3.2% increase in $[\text{OH}]_{\text{gm}}$, and 3.6% decrease in CH_4
lifetime. The impact of cloud heterogeneous reactions matches the results of Holmes et al. (2019), but the impact of
aerosol heterogeneous reactions is a bit larger, which may reflect differences in surface area density fields and the
uptake coefficients of N_2O_5 on organic carbon, sea salt and sulfate surface. Neglecting the full impact of heterogeneous
460 reactions results in a 5.8% increase in $[\text{OH}]_{\text{gm}}$ and 5.2% decrease in CH_4 lifetime.

The radical terminating, termolecular reaction between OH and NO_2 exerts substantial influence on the lifetime of NO_x
and on tropospheric OH. However, there is uncertainty over the reaction pathways involved, and recent kinetic
recommendations have distinguished the dominant pathway forming nitric acid and a secondary pathway forming
HOONO (e.g., Burkholder et al., 2020). Models not representing HOONO may consider this species to behave as nitric
465 acid or to decompose rapidly to OH and NO_2 . In our control run we have assumed the former, using the recent
assessments of the rate coefficients of Amedro et al. (2019, 2020), supported by the study of Rolletter et al. (2025). In
our JPL run we have assumed the latter, using rate coefficients for the pathway forming nitric acid only (Burkholder et
al., 2020). As **Figure 7f** shows, the faster rate coefficient in the control run than in the JPL run leads to an 8% decrease
in tropospheric OH concentration, especially in the upper troposphere and at high latitudes. Global mean $[\text{OH}]_{\text{gm}}$
470 decreases by 7%, leading to an 8.4% increase in CH_4 lifetime.

4.2 Tropospheric OH budgets

In this section, we quantify the factors affecting the major sources and sinks of OH. The primary source of OH is the
photolysis of ozone (O_3) at wavelengths less than 330 nm, which produces electronically excited oxygen atoms ($\text{O}(^1\text{D})$).
Some of these atoms subsequently react with water vapor to form OH. In the control run (CTL, **Table 4**), this pathway
475 accounts for $92 \text{ Tmol}\cdot\text{year}^{-1}$, or 44% of total OH production—closely matching estimates from Lelieveld et al. (2016)
and Bossolasco et al. (2025). Other significant production pathways include the reaction of HO_2 with NO (33%), HO_2
with O_3 (13%), and photolysis of hydrogen peroxide (H_2O_2 , 8%). Minor contributions arise from photolysis of VOCs
and organic hydroperoxides (ROOH), as well as other trace pathways. On the loss side, the dominant sink is the
reaction of OH with carbon monoxide (CO), contributing to 41% of total OH removal in the control run. This is
480 consistent with the contribution of approximately ~40% reported by Fiore et al. (2024). Additional important sinks
include reactions with CH_4 (15%), non-methane VOCs and ROOH (15%), and aldehydes (RCHO, 8%). Reactions with
 O_3 and NO_x account for 7%, while minor reactions contribute the remaining 14%.

Comparison of the fixEmis run with the control run indicates that the variation in emissions from year to year has a
relatively minor impact on OH production and loss. Neglecting UV absorption by water vapor (noWVA) results in 5
485 $\text{Tmol}\cdot\text{year}^{-1}$ greater OH production via the primary pathway ($\text{O}(^1\text{D})+\text{H}_2\text{O}$) due to strong solar radiation. Heterogeneous
reactions significantly influence the HO_2+NO and HO_2+O_3 pathways, increasing production by approximately 4
 $\text{Tmol}\cdot\text{year}^{-1}$ and 3 $\text{Tmol}\cdot\text{year}^{-1}$, respectively. However, their relative contributions to total OH production remain largely
unchanged. Neglecting the HOONO channel associated with the $\text{OH}+\text{NO}_2$ reaction results in a modest decrease in OH



490 loss, from 2.3 Tmol·year⁻¹ to 2.1 Tmol·year⁻¹. This reduction contributes to net OH accumulation, increasing total OH production from 208 Tmol·year⁻¹ to 217 Tmol·year⁻¹, primarily through the O(¹D)+H₂O, HO₂+NO, and HO₂+O₃ pathways. Overall, the sensitivity experiments highlight the key atmospheric processes influencing OH levels and quantify their respective impacts.

Table 4. Main reactions leading to tropospheric production and loss of OH (Tmol·year⁻¹) and their relative contribution (%) in seven experiments.

	CTL	fixEmis	noWVA	noCloud	noAero	noHete	JPL
Production							
O(¹ D)+H ₂ O	92(44%)	91(44%)	96(45%)	92(44%)	92(43%)	93(43%)	95(44%)
HO ₂ +NO	68(33%)	67(33%)	69(32%)	70(33%)	71(33%)	72(33%)	72(33%)
HO ₂ +O ₃	26(13%)	26(13%)	26(12%)	27(13%)	28(13%)	29(13%)	28(13%)
H ₂ O ₂ +hv	17(8%)	17(8%)	18(8%)	17(8%)	18(9%)	19(9%)	17(8%)
VOCs,ROOH+hv	4.1(2.0%)	3.9(1.9%)	4.2(1.9%)	4.1(1.9%)	4.1(1.9%)	4.1(1.9%)	4.0(1.8%)
other	0.4(0.2%)	0.3(0.2%)	0.3(0.2%)	0.3(0.2%)	0.4(0.2%)	0.4(0.2%)	0.3(0.2%)
Total	208	205	213	210	214	217	217
Loss							
OH+CO	86(41%)	84(41%)	87(41%)	87(41%)	87(41%)	88(40%)	88(41%)
OH+CH ₄	32(15%)	32(16%)	33(16%)	32(15%)	33(15%)	34(15%)	34(16%)
OH+VOCs, ROOH	32(15%)	31(15%)	32(15%)	32(15%)	32(15%)	33(15%)	32(15%)
OH+RCHO	16(8%)	16(8%)	17(8%)	17(8%)	17(8%)	17(8%)	18(8%)
OH+O ₃	11(6%)	11(6%)	12(5%)	12(6%)	12(6%)	12(6%)	13(6%)
OH+NO ₂	2.3(1.1%)	2.2(1.1%)	2.3(1.1%)	2.3(1.1%)	2.4(1.1%)	2.5(1.1%)	2.1(1.0%)
other	28(14%)	28(14%)	29(14%)	29(14%)	30(14%)	31(14%)	30(14%)
Total	208	205	213	210	214	217	217

495 **4.3 Impact of oceanic CH₃CHO emissions**

Previous studies have indicated that oceanic emissions of CH₃CHO represent a missing sink of OH in current chemistry-climate models (Wang et al, 2019). Due to the limited measurement data and large uncertainty in these emissions, we conducted two additional short simulation experiments to assess their impacts on [OH]_{gm}. **Figure 8** shows the vertical distribution of CH₃CHO measured over the remote Pacific during the ATom campaigns, as well as model mixing ratios sampled along the flight tracks. Without oceanic emissions (CTL run), the model underestimated CH₃CHO by up to an order of magnitude in the boundary layer and free troposphere (see **Figure 8**). By including oceanic emissions, simulated CH₃CHO in the marine boundary layer is greatly improved, with the mean bias reduced from ~100 pptv to ~20 pptv, especially in spring and summer. However, the subsequent impact in the free troposphere is relatively limited, indicating that that an additional missing chemical source likely exists there, as suggested by Wang et al., (2019).

500

505

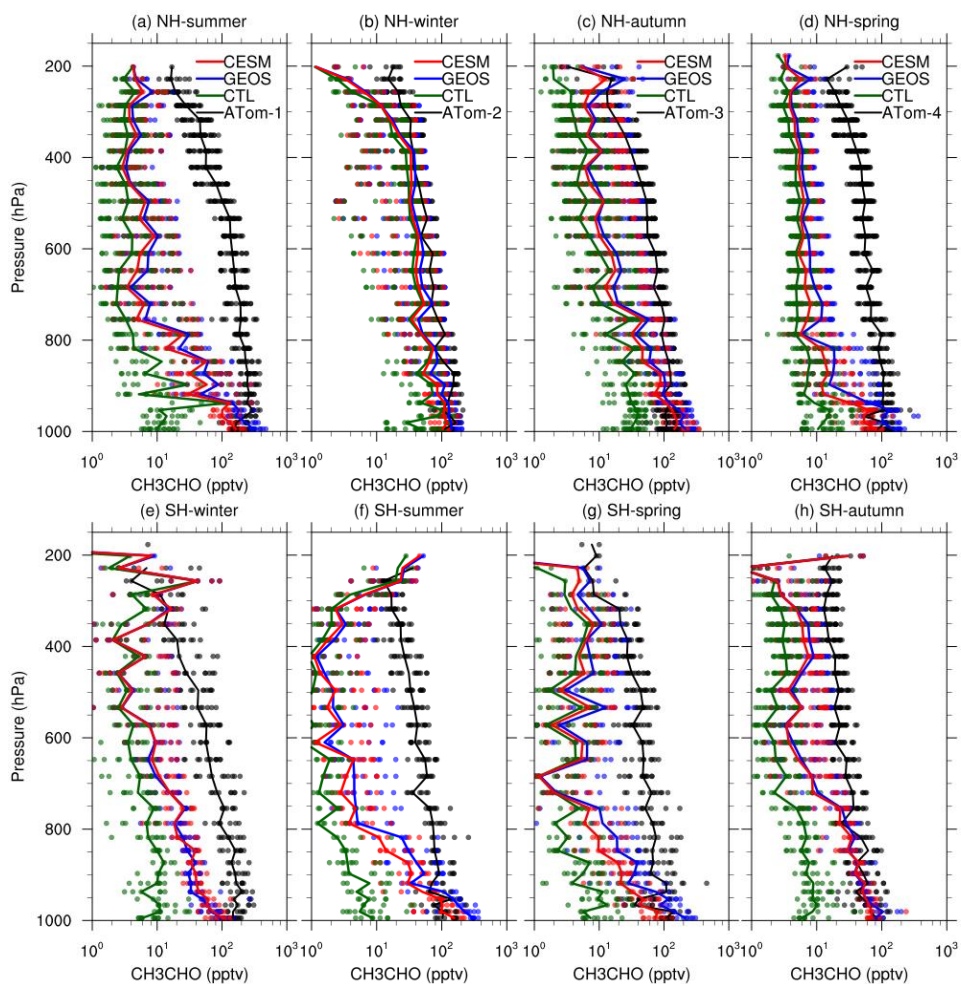


Figure 8. As Figure 5, but for CH₃CHO (pptv). The model control run (CTL) is shown in green, with results from model runs using emissions from CESH and GEOS-Chem shown in red and blue respectively.

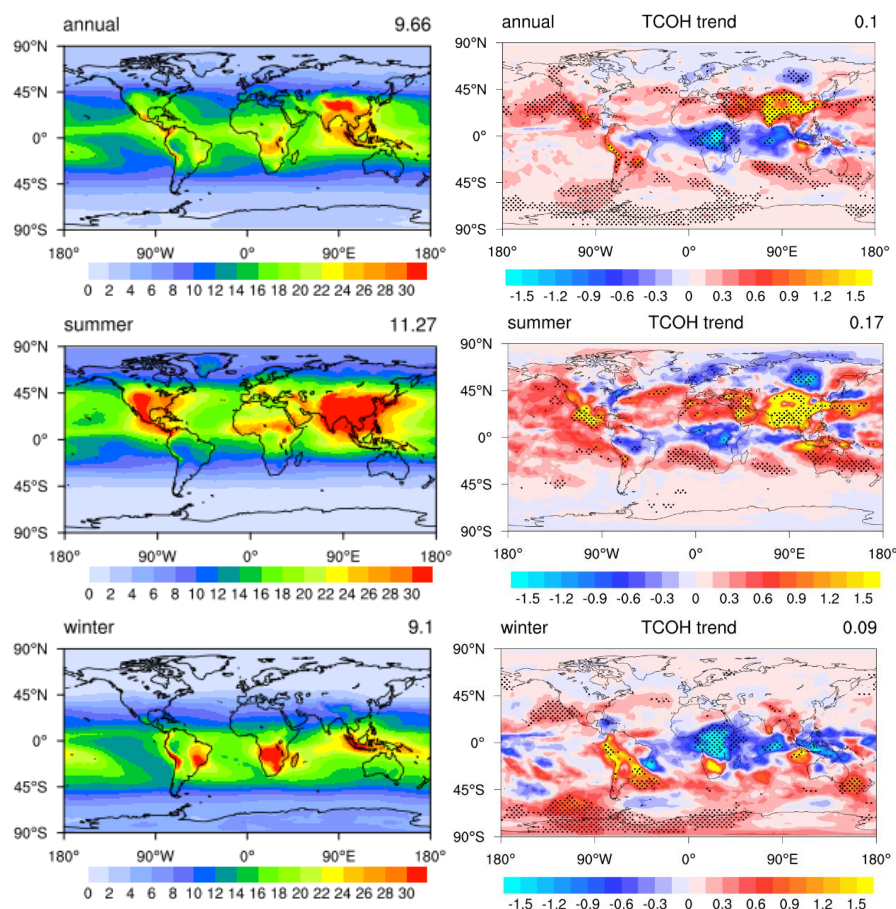
Table 5. The annual mean global emissions and burdens of CH₃CHO, [OH]_{gm} and τ_{CH₄} during 2016-2017 from ALD-cesm and ALD-geoc runs

	Millet et al. (2010)	CTL	ALD-cesm	ALD-geoc
Ocean emissions (Tg·yr ⁻¹)	57	/	40.8	62.7
Other emissions (Tg·yr ⁻¹)	28	28.2	28.2	28.2
Total emissions (Tg·yr ⁻¹)	85	28.2	69.0	90.9
CH ₃ CHO burden (Tg)	0.5	0.32	0.38	0.42
[OH] _{gm} (molecules·cm ⁻³)	/	10.94	10.84	10.78
τ _{CH₄} (years)	/	9.82	9.92	9.98



As shown in **Table 5**, including oceanic emissions of CH_3CHO increases its global burden from 0.32 Tg to 0.38 Tg (+19%) in the ALD-cesm run, and to 0.42 Tg (+31%) in the ALD-geoc run—bringing the simulated values into much closer agreement with previous estimates (e.g. Millet et al., 2010), and thereby improving confidence in the representation of CH_3CHO sources in the model. This increase in CH_3CHO leads to a decrease in the global mean OH concentration of up to 1.5% and an increase in the CH_4 lifetime up to 9.98 years (+1.6%). Overall, while current estimates of oceanic CH_3CHO emissions slightly decrease global mean OH concentration and marginally increase CH_4 lifetime, their impact appears limited. Nonetheless, incorporating more reliable oceanic CH_3CHO emission estimates and improving the representation of its sources in the free troposphere may lead to a stronger impact of CH_3CHO on $[\text{OH}]_{\text{gm}}$ and τ_{CH_4} .

520 4.4 Tropospheric OH column trends



525 **Figure 9.** The tropospheric column of OH (TCOH, 10^{12} molecules \cdot cm $^{-2}$, left panels) and the trend (10^{11} molecules \cdot cm $^{-2}$ \cdot yr $^{-1}$, right panels) in annual, winter and summer from 2000 to 2017. The troposphere was defined as the region below a climatological tropopause ($p = 300 - 215(\cos(\text{lat}))^2$) following Lawrence et al. (2001). Trends are calculated as in Figure 1. The value in the right corner is the global average.



The annual and seasonal distribution of tropospheric column OH exhibits substantial spatial and seasonal heterogeneity (Figure 9). In summer, the highest columns are located in low and mid latitudes of the northern hemisphere, while in winter they are located in the southern hemisphere. Maxima are primarily located in the Northern Hemisphere in regions where anthropogenic emissions dominate the high OH production (e.g., India, China, Southeast Asia, and Central America). Regions of high tropospheric OH column are primarily associated with elevated levels of OH precursors, particularly NO₂, and the short lifetime of OH further confines its distribution and limits long-range transport (Duncan et al., 2016; Chua et al., 2023). Over tropical oceans, there are relatively high columns which may be attributed to high primary production and NO_x shipping emissions, as evidenced by column maxima along shipping lanes between Sri Lanka and Malaysia (Richter et al., 2004). Another broad column maximum extends across the Atlantic Ocean, a likely result of influence from African and South American biomass burning.

The trends in the annual tropospheric OH column also exhibit large spatial heterogeneity (Figure 9, right panels). Increases in OH of up to 0.3×10^{11} molecules·cm⁻²·yr⁻¹ dominate over most of the world, particularly over India and China where they exceed 1.5×10^{11} molecules·cm⁻²·yr⁻¹ (1.6%·yr⁻¹), although there are large, coherent regions showing decreases in OH, typically of 0.3×10^{11} molecules·cm⁻²·yr⁻¹, particularly over central Africa, the tropical Atlantic and Indian Oceans where the decrease exceeds 1%·yr⁻¹. When averaged globally, these regional distinctions are lost, and there is a net increase of 0.1×10^{11} molecules·cm⁻²·yr⁻¹. Over India and China, the increases are significant and are closely linked to the increased emissions of NO_x and other O₃ precursors (Hou et al., 2023), although small increases are still seen in the fixed-emission experiment. Over tropical Africa there are decreases in OH whether or not emission changes are considered, suggesting that they arise from changes in meteorology rather than emissions. However, we note that the modelled increase in CO column in this region may lead to an overestimation of the decreases in OH over Africa and the tropical oceans.

4.5 Contributions of Key Processes to Tropospheric OH Variability and Trends

We quantify the relative contributions of key factors to changes in annual global mean OH over time by comparing sensitivity simulations with the control run. Meteorological effects are estimated using simulations with fixed emissions, which isolate variability driven by meteorology. The control simulation is used as a reference to represent the combined influence of all processes.

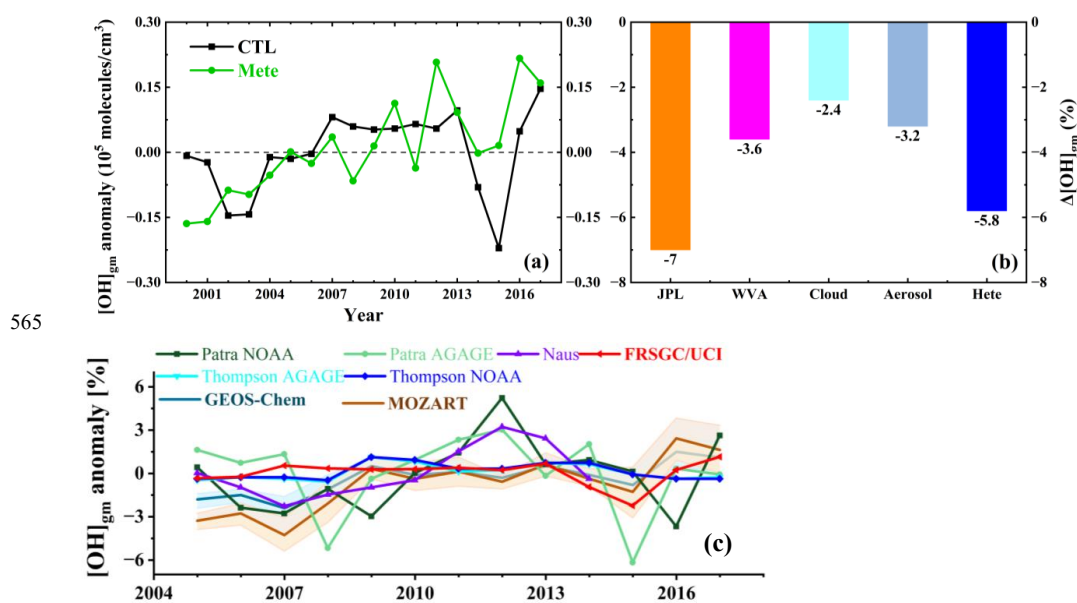
Table 6. Annual and seasonal [OH]_{gm} trends (10³ molecules·cm⁻³·yr⁻¹) in seven simulation experiments.

	CTL	fixEmis	noWVA	noCloud	noAero	noHete	JPL
Annual	0.74	1.69	0.85	0.83	0.74	0.83	0.79
Spring	0.72*	1.29	0.78*	0.75*	0.7*	0.72*	0.73*
Summer	1.36	2.24	1.48	1.42	1.29	1.34	1.39
Autumn	0.52**	1.29	0.55**	0.63**	0.45**	0.54**	0.51**
Winter	0.32**	1.44	0.33**	0.43**	0.3**	0.37**	0.35**

Note: Trends are calculated using the Theil–Sen method. Trends with * are not significant at a 90% level using the Mann–Kendall test, but are at an 80% level. ** indicate trends that are not significant at an 80% level. Bold values indicate the maximum trend in each experiment.



Most observational estimates based on methyl chloroform (MCF) indicate a decrease in global mean OH from about 2005 (Rigby et al., 2017) but estimates from atmospheric chemistry transport models typically suggest an increase over this period (Stevenson et al., 2020; Zhao et al., 2020). Our simulated OH shows relatively little change from 2000 to 2017, with a small net increase of 0.74×10^3 molecules·cm⁻³·yr⁻¹ (6.8%·yr⁻¹ of the multiyear global mean OH, see **Table 6 and Figure 10c**). In summer, the increases are largest at 1.36×10^3 molecules·cm⁻³·yr⁻¹ and are significant. Changes in meteorological conditions alone lead to a larger increase of 1.69×10^3 molecules·cm⁻³·yr. In autumn and winter, the OH increase by 0.52×10^3 and 0.32×10^3 molecules·cm⁻³·yr⁻¹, respectively, but these increases are not statistically significant.



565

Figure 10. (a) The anomaly of $[OH]_{gm}$ (10^5 molecules·cm⁻³) in the control run and fixed emission run, (b) the average relative differences in $[OH]_{gm}$ from the control run (%) from 2000 to 2017, and (c) comparison of $[OH]_{gm}$ anomalies (%) from this work (FRSGC/UCI) and other studies. The labels in panel (b) match those in Figure 7.

As shown in **Figure 10a**, there is a slight increase in global mean OH from 2006 to 2007 and decreases in 2002 and 2015 in the control run. The 2007 increase can be attributed to anomalously low fire-related CO emissions associated with the La Niña event (**Figure S3**; Zhao et al., 2025). This reduction in CO emissions led to lower global CO concentrations, thereby decreasing OH consumption via the OH + CO reaction pathway. In contrast, both 2002 and 2015 experienced elevated fire emissions—particularly in 2015—driven by intensified tropical wildfires linked to El Niño events, resulting in increased atmospheric CO and enhanced OH loss. These variations are not present in the run with fixed emissions, providing further evidence that interannual changes in fire-related CO emissions significantly influence OH.

Although water vapor UV absorption and heterogeneous reactions significantly influence the absolute global abundance of OH, they have a limited effect on its trend. Most chemistry-climate models tend to overestimate OH. Incorporating processes such as water vapor UV absorption and heterogeneous reactions involving N₂O₅, HO₂, NO₂ and NO₃ can effectively reduce this overestimation without substantially altering the OH trend, thereby improving model

580



performance. As shown in **Table 6** and **Figure 10**, water vapor UV absorption reduces global mean OH by 3.6% and slightly weakens its increase. Heterogeneous chemistry on clouds decreases OH by 2.4% and also suppresses the increase trend, while aerosols reduce OH by 3.2% but have little influence on the interannual variations. The combined
585 heterogeneous effect leads to a 5.8% reduction in global mean OH, largely driven by cloud processes. In contrast, although the OH + NO₂ reaction contributes only ~1% to total OH loss, small changes in its rate can induce up to 7% changes in global mean OH, with minimal impact on the long-term trend.

Tropospheric OH variations in **Figure 10 (c)** calculated using the FRSGC/UCI CTL run from 2005 to 2017 are compared with those derived from the MOZART (brown) and GEOS-Chem (navy) models as reported by Zhao et al.
590 (2025). Also shown in **Figure (c)** are MCF-based inversions from the 3D model outlined by Patra et al. (2021) and Naus et al. (2019), as well as the HFC-based inversions from the box model described by Thompson et al. (2024). The behavior of the FRSGC/UCI model is broadly consistent with the GEOS-Chem and MOZART simulations, as well as the MCF- and HFC-based inversion estimates. Most datasets capture similar temporal features, including enhanced OH around 2012–2013 and lower values during 2014–2015, although the magnitude of variability differs considerably. In
595 particular, the MCF-based inversions exhibit substantially larger year-to-year fluctuations than both the chemistry transport models and the HFC-based inversions. The spread among estimates highlights the uncertainties associated with different observational constraints, inversion frameworks, chemical mechanisms, and transport processes. Nevertheless, the overall agreement among these independent approaches supports the conclusion that global tropospheric OH remained relatively stable over the study period.

600 **5 Conclusions**

This study has analyzed the distribution and evolution of tropospheric OH and of its sensitivity to key factors from 2000 to 2017 using an updated version of the FRSGC/UCI global chemistry transport model. The model reproduces the observed distribution and interannual changes in the tropospheric O₃ column and tropospheric NO₂ column well but does not capture the observed decrease in the CO column. This mismatch in the CO trend may lead to an
605 underestimation of any increase or overestimation of any decrease in OH concentrations over the 2000–2017 period. The model captures the vertical profile of OH relatively well in oceanic regions, although HO₂ is overestimated in the mid troposphere, highlighting potential chemical biases or weaknesses in emissions estimates.

Airmass-weighted OH concentrations and methane lifetimes in this study are fully consistent with observational and multi-model estimates. There are relatively high OH concentrations between 30°S and 30°N in the lower to middle
610 troposphere, with largest values in the northern hemisphere. The contributions of water vapor absorption and heterogeneous reactions on aerosol decrease with altitude, while the effect of heterogeneous reactions on cloud droplets peaks in the upper troposphere. A slower reaction rate for the termolecular reaction between OH and NO₂ leads to a 7% increase in global tropospheric OH that is largest in the upper troposphere and at high latitudes. UV absorption by water vapor results in a 4.3% decrease in OH production via the primary pathway (O(¹D) + H₂O). Heterogeneous reactions
615 reduce OH concentrations by suppressing the HO₂+NO and HO₂+O₃ pathways, primarily through the depletion of HO₂ and the alteration of NO_x partitioning, both of which are closely linked to ambient NO_x and HO₂ levels.



The tropospheric OH column exhibits substantial spatial and seasonal variability and shows a significant positive trend over most regions of the globe. The largest increases are found over India and China, exceeding $1.5 \times 10^{11} \text{ molec}\cdot\text{cm}^{-2}\cdot\text{yr}^{-1}$ ($>1.6\%\cdot\text{yr}^{-1}$) which can principally be attributed to the increase in anthropogenic emissions. In contrast, decreases
620 in the OH column is evident over tropical regions, approximately $-0.3 \times 10^{10} \text{ molec}\cdot\text{cm}^{-2}\cdot\text{yr}^{-1}$, particularly in tropical Africa, the tropical Atlantic and the Indian Ocean where decreases exceed $1\%\cdot\text{yr}^{-1}$. These decreases reflect changes in meteorological conditions (contributing $\sim 60\%$) but also reflect a mismatch in the modelled CO column trend ($\sim 16\%$). The annual trend in global mean OH exhibits a weak but statistically significant positive trend, particularly in summer, averaging $1.36 \times 10^3 \text{ molec}\cdot\text{cm}^{-3}\cdot\text{yr}^{-1}$. This is likely associated with changes in NO_x emissions. Meteorological variability
625 contributes to a more significant increase in global mean OH of $1.69 \times 10^3 \text{ molec}\cdot\text{cm}^{-3}\cdot\text{yr}^{-1}$.

While water vapor UV absorption and heterogeneous reactions have a limited influence on the interannual variability of global mean OH, they substantially affect its absolute level. Specifically, water vapor UV absorption reduces global mean OH by 3.6%, increasing the methane lifetime by 4.2%. The combined influence of cloud- and aerosol-related heterogeneous processes leads to an overall 5.8% decrease in global mean OH. Incorporating these processes reduces
630 the simulated OH levels without substantially altering its long-term trend, thereby improving model performance, consistent with previous studies. The 7% decrease of OH by faster OH + NO_2 reaction induces an 8.4% change in methane lifetime, underscoring the importance of accurately representing termolecular reaction kinetics. Oceanic acetaldehyde emissions ($40\text{--}63 \text{ Tg}\cdot\text{yr}^{-1}$) lead to modest reductions in OH (0.9–1.5%) and increases in methane lifetime (1.0–1.6%), highlighting the role of biogenic source uncertainties. Overall, these findings underscore the sensitivity of
635 the atmospheric oxidative capacity to both chemical processes and emission uncertainties, with direct implications for methane lifetime. Improved representation of these processes is essential for reliable projections of future air quality and climate.

Data availability

The monthly mean model outputs used in this study are publicly available at <https://zenodo.org/uploads/19112214>. The
640 Aura Ozone Monitoring Instrument/Microwave Limb Sounder (OMI/MLS) tropospheric ozone dataset was obtained from https://acd-ext.gsfc.nasa.gov/Data_services/cloud_slice/new_data.html (last access: 20 March 2026). Tropospheric NO_2 column data from OMI QA4ECV version 1.1 for the period 2005–2017 were provided by the Tropospheric Emission Monitoring Internet Service (TEMIS; <https://www.temis.nl/>, last access: 20 March 2026). MOPITT-derived CO (Near- and Thermal-Infrared Radiances), version 9 (V009), for 2001–2017 were obtained from the NASA Earthdata
645 archive (<https://asdc.larc.nasa.gov/project/MOPITT>, last access: 20 March 2026). The gridded Tropospheric Ozone Assessment Report (TOAR) global database is available at <https://doi.pangaea.de/10.1594/PANGAEA.880506> (last access: 20 March 2026). Vertical profiles of OH, HO_2 , and CH_3CHO from the Atmospheric Tomography Mission (ATom) were obtained from the NASA Earthdata archive (<https://www.earthdata.nasa.gov/data/catalog/ornl-cloud-atom-merge-v2-1925-2.0>, last access: 20 March 2026).

650 **Author contributions**



XH, RH and OW designed the study. RH processed the emission inventories. XH, RH, OW and AM updated model code. RP and XH created codes to compare model outputs with satellite data using averaging kernels. XH ran model simulations and performed the analysis. XH and RH prepared the paper with contributions from all co-authors. SW provided seawater acetaldehyde concentrations and guidance for configuring the CESM2 simulations. XH and YW
655 conducted CESM2 and GEOS-Chem model runs to generate oceanic acetaldehyde emissions. YZ contributed OH anomaly data derived from MOZART and the GEOS-Chem chemical mechanisms. OW, JL, BZ, TZ and AP discussed the results and offered valuable comments.

Competing interests

James Lee is an editor of Atmospheric Chemistry and Physics. The authors declare that they have no other competing
660 interests.

Acknowledgements

We acknowledge the use of the High-End Computing (HEC) high performance and high throughput computing resources at Lancaster University, UK, as well as additional computational support from High-Performance Computing Center at Nanjing University of Information Science & Technology, China. We also thank Louisa Emmons from the
665 NSF National Center for Atmospheric Research for valuable advice on the implementation and operation of the CESM2-OASISS module (<https://wiki.ucar.edu/spaces/camchem/pages/358319521/Online+Air-Sea+Interface+for+Soluble+Species+OASISS>).

Financial support

XH is supported by the National Key Research and Development Program of China (grant no. 2022YFC3701204). RH
670 and XH are supported by the NERC grant LSO3 (NE/V011863/1). RH and AM are supported by the NERC InHALE grant (NE/X003582/). RP was funded by the UK Natural Environment Research Council (NERC) by providing funding for the National Centre for Earth Observation (NCEO, award reference NE/R016518/1).

References

- Amedro, D., Bunkan, A. J. C., Berasategui, M., and Crowley, J. N.: Kinetics of the OH + NO₂ reaction: rate coefficients
675 (217–333 K, 16–1200 mbar) and fall-off parameters for N₂ and O₂ bath gases, *Atmos. Chem. Phys.*, 19, 10643–10657, <https://doi.org/10.5194/acp-19-10643-2019>, 2019.
- Amedro, D., Berasategui, M., Bunkan, A. J. C., Pozzer, A., Lelieveld, J., and Crowley, J. N.: Kinetics of the OH + NO₂ reaction: effect of water vapour and new parameterization for global modelling, *Atmos. Chem. Phys.*, 20, 3091–3105, <https://doi.org/10.5194/acp-20-3091-2020>, 2020.
- 680 Anderson, D. C., Duncan, B. N., Liu, J., Nicely, J. M., Strode, S. A., Follette-Cook, M. B., Souri, A. H., Ziemke, J. R., González-Abad, G., Ayazpour, Z.: Trends and interannual variability of the hydroxyl radical in the remote tropics during



- boreal autumn inferred from satellite proxy data, *Geophys. Res. Lett.*, 51, e2024GL108531, <https://doi.org/10.1029/2024GL108531>, 2024.
- 685 Anderson, D. C., Duncan, B. N., Fiore, A. M., Baublitz, C. B., Follette-Cook, M. B., Nicely, J. M., and Wolfe, G. M.: Spatial and temporal variability in the hydroxyl (OH) radical: understanding the role of large-scale climate features and their influence on OH through its dynamical and photochemical drivers, *Atmos. Chem. Phys.*, 21, 6481–6508, <https://doi.org/10.5194/acp-21-6481-2021>, 2021.
- 690 Archibald, A. T., O'Connor, F. M., Abraham, N. L., Archer-Nicholls, S., Chipperfield, M. P., Dalvi, M., Folberth, G. A., Dennison, F., Dhomse, S. S., Griffiths, P. T., Hardacre, C., Hewitt, A. J., Hill, R. S., Johnson, C. E., Keeble, J., Köhler, M. O., Morgenstern, O., Mulcahy, J. P., Ordóñez, C., Pope, R. J., Rumbold, S. T., Russo, M. R., Savage, N. H., Sellar, A., Stringer, M., Turnock, S. T., Wild, O., and Zeng, G.: Description and evaluation of the UKCA stratosphere–troposphere chemistry scheme (StratTrop vn 1.0) implemented in UKESM1, *Geosci. Model Dev.*, 13, 1223–1266, <https://doi.org/10.5194/gmd-13-1223-2020>, 2020.
- 695 Atkinson, R., Baulch, D. L., Cox, R. A., Jr. Hampson, R. F., Kerr, J. A., Troe, J.: Evaluated Kinetic and Photochemical Data for Atmospheric Chemistry: Supplement IV. IUPAC Subcommittee on Gas Kinetic Data Evaluation for Atmospheric Chemistry, *J. Phys. Chem. Ref. Data* 21, 1125, <https://doi.org/10.1063/1.555918>, 1992
- 700 Boersma, K. F., Eskes, H. J., Richter, A., De Smedt, I., Lorente, A., Beirle, S., van Geffen, J. H. G. M., Zara, M., Peters, E., Van Roozendael, M., Wagner, T., Maasakkers, J. D., van der A, R. J., Nightingale, J., De Rudder, A., Irie, H., Pinardi, G., Lambert, J.-C., and Compernelle, S. C.: Improving algorithms and uncertainty estimates for satellite NO₂ retrievals: results from the quality assurance for the essential climate variables (QA4ECV) project, *Atmos. Meas. Tech.*, 11, 6651–6678, <https://doi.org/10.5194/amt-11-6651-2018>, 2018.
- Bossolasco, A., Fernandez, R. P., Li, Q., Mahajan, A. S., Villamayor, J., Barrera, J. A., Heard, D. E., Cuevas, C. A., Caram, C., Szopaj, S. and Saiz-Lopez, A.: Key role of short-lived halogens on global atmospheric oxidation during historical periods, *Environ. Sci.: Atmos.*, <https://doi.org/10.1039/d4ea00141a>, 5, 547, 2025.
- 705 Bozzo, A., Benedetti, A., Flemming, J., Kipling, Z., and Rémy, S.: An aerosol climatology for global models based on the tropospheric aerosol scheme in the Integrated Forecasting System of ECMWF, *Geosci. Model Dev.*, 13, 1007–1034, <https://doi.org/10.5194/gmd-13-1007-2020>, 2020.
- Brasseur, G. P. and Solomon, S.: *Aeronomy of the Middle Atmosphere*, Springer Netherlands, <https://doi.org/10.1007/1-4020-3824-0>, 2005.
- 710 Brune, W. H., Miller, D. O., Thames, A. B., Allen, H. M., Apel, E. C., Blake, D. R., Bui, T. P., Commane, R., Crouse, J. D., Daube, B. C., Diskin, G. S., DiGangi, J. P., Elkins, J. W., Hall, S. R., Hanisco, T. F., Hannun, R. A., Hints, E. J., Hornbrook, R. S., Kim, M. J., McKain, K., Moore, F. L., Neuman, J. A., Nicely, J. M., Peischl, J., Ryerson, T. B., St. Clair, J. M., Sweeney, C., Teng, A. P., Thompson, C., Ullmann, K., Veres, P. R., Wennberg, P. O., and Wolfe, G. M.: Exploring Oxidation in the Remote Free Troposphere: Insights From Atmospheric Tomography (ATom), *J. Geophys. Res. Atmos.*, 125, e2019JD031685, <https://doi.org/10.1029/2019JD031685>, 2020.
- 715 Burkholder, J. B., Sander, S. P., Abbatt, J., Barker, J. R., Cappa, C., Crouse, J. D., Dibble, T. S., Huie, R. E., Kolb, C. E., Kurylo, M. J., Orkin, V. L., Percival, C. J., Wilmouth, D. M., and Wine, P. H.: *Chemical Kinetics and Photochemical Data for Use in Atmospheric Studies*, Evaluation No. 19, JPL Publication 19-5, Jet Propulsion Laboratory, Pasadena, <https://dataverse.jpl.nasa.gov/dataset.xhtml?persistentId=hdl:2014/49199&version=2.1>, May 1, 2020.
- 720 Cantrell, C. A., Shetter, R. E., Gilpin, T. M., Calvert, J. G., Eisele, F. L., and Tanner, D. J.: Peroxy radical concentrations measured and calculated from trace gas measurements in the Mauna Loa observatory photochemistry experiment 2, *J. Geophys. Res.-Atmos.*, 101, 14653–14664, <https://doi.org/10.1029/95JD03613>, 1996.
- Christian, K. E., Brune, W. H., Mao, J., and Ren, X.: Global sensitivity analysis of GEOS-Chem modeled ozone and



- hydrogen oxides during the INTEX campaigns, *Atmos. Chem. Phys.*, 18, 2443–2460, <https://doi.org/10.5194/acp-18-2443-2018>, 2018.
- 725
- Chua, G., Naik, V., and Horowitz, L. W.: Exploring the drivers of tropospheric hydroxyl radical trends in the Geophysical Fluid Dynamics Laboratory AM4.1 atmospheric chemistry–climate model, *Atmos. Chem. Phys.*, 23, 4955–4975, <https://doi.org/10.5194/acp-23-4955-2023>, 2023.
- Compernelle, S., Verhoelst, T., Pinardi, G., Granville, J., Hubert, D., Keppens, A., Niemeijer, S., Rino, B., Bais, A., Beirle, S., Boersma, F., Burrows, J. P., De Smedt, I., Eskes, H., Goutail, F., Hendrick, F., Lorente, A., Pazmino, A., PETERS, A., Peters, E., Pommereau, J.-P., Remmers, J., Richter, A., van Geffen, J., Van Roozendael, M., Wagner, T., and Lambert, J.-C.: Validation of Aura-OMI QA4ECV NO₂ climate data records with ground-based DOAS networks: the role of measurement and comparison uncertainties, *Atmos. Chem. Phys.*, 20, 8017–8045, <https://doi.org/10.5194/acp-20-8017-2020>, 2020.
- 730
- Crowley, J. N., Ammann, M., Cox, R. A., Hynes, R. G., Jenkin, M. E., Mellouki, A., Rossi, M. J., Troe, J., and Wallington, T. J.: Evaluated kinetic and photochemical data for atmospheric chemistry: Volume V – heterogeneous reactions on solid substrates, *Atmos. Chem. Phys.*, 10, 9059–9223, <https://doi.org/10.5194/acp-10-9059-2010>, 2010.
- 735
- Crutzen, P. J.: The Role of NO and NO₂ in the Chemistry of the Troposphere and Stratosphere, *Annual Review of Earth and Planetary Sciences*, 7, 443–472, 1979.
- 740
- Deeter, M., Francis, G., Gille, J., Mao, D., Martínez-Alonso, S., Worden, H., Ziskin, D., Drummond, J., Commane, R., Diskin, G., and McKain, K.: The MOPIIT Version 9 CO product: sampling enhancements and validation, *Atmos. Meas. Tech.*, 15, 2325–2344, <https://doi.org/10.5194/amt-15-2325-2022>, 2022.
- Duncan, B. N., Lamsal, L. N., Thompson, A. M., Yoshida, Y., Lu, Z. F., Streets, D. G., Hurwitz, M. M., Pickering, K. E.: A space-based, high-resolution view of notable changes in urban NO_x pollution around the world (2005–2014), *J. Geophys. Res.*, 121(2), 976–996, <https://doi.org/10.1002/2015jd024121>, 2016.
- 745
- Duncan, B. N., Anderson, D. C., Fiore, A. M., Joiner, J., Krotkov, N. A., Li, C., Millet, D. B., Nicely, J. M., Oman, L. D., St. Clair, J. M., Shutter, J. D., Souri, A. H., Strode, S. A., Weir, B., Wolfe, G. M., Worden, H. M., and Zhu, Q.: Opinion: Beyond global means – novel space-based approaches to indirectly constrain the concentrations of and trends and variations in the tropospheric hydroxyl radical (OH), *Atmos. Chem. Phys.*, 24, 13001–13023, <https://doi.org/10.5194/acp-24-13001-2024>, 2024.
- 750
- Elshorbany, Y., Ziemke, J. R., Strode, S., Petetin, H., Miyazaki, K., De Smedt, I., Pickering, K., Seguel, R. J., Worden, H., Emmerichs, T., Taraborrelli, D., Cazorla, M., Fadnavis, S., Buchholz, R. R., Gaubert, B., Rojas, N. Y., Nogueira, T., Salameh, T., and Huang, M.: Tropospheric ozone precursors: global and regional distributions, trends, and variability, *Atmos. Chem. Phys.*, 24, 12225–12257, <https://doi.org/10.5194/acp-24-12225-2024>, 2024.
- 755
- Emmons, L. K., Schwantes, R. H., Orlando, J. J., Tyndall, G., Kinnison, D., Lamarque, J., Marsh, D., Mills, M. J., Tilmes, S., Bardeen, C., Buchholz, R. R., Conley, A., Gettelman, A., Garcia, R., Simpson, I., Blake, D. R., Meinardi, S., and Pétron, G.: The Chemistry Mechanism in the Community Earth System Model Version 2 (CESM2), *J. Adv. Model. Earth Sy.*, 12, e2019MS001882, <https://doi.org/10.1029/2019MS001882>, 2020.
- Fei, D. D., Hou, X. W., Wei, L.: Quantitative sources of global surface ozone and spatial and temporal distribution characteristics, *China Environmental Science*, 41(7): 3004–3016, <https://doi.org/10.0000/j.zghjxk.1000-6923.20214117627>, 2021.
- 760
- Fiore, A. M., Dentener, F. J., Wild, O., Cuvelier, C., Schultz, M. G., Hess, P., Textor, C., Schulz, M., Doherty, R. M., Horowitz, L. W., MacKenzie, A., Sanderson, M. G., Shindell, D. T., Stevenson, D. S., Szopa, S., Van Dingenen, R., Zeng, G., Atherton, C., Bergmann, D., Bey, I., Carmichael, G., Collins, W. J., Duncan, B. N., Faluvegi, G., Folberth, G., Gauss, M., Gong, S., Hauglustaine, D., Holloway, T., Isaksen, I. S. A., Jacob, D. J., Jonson, J. E., Kaminski, J. W.,



- Keating, T. J., Lupu, A., Marmer, E., Montanaro, V., Park, R. J., Pitari, G., Pringle, K. J., Pyle, J. A., Schroeder, S., Vivanco, M. G., Wind, P., Wojcik, G., Wu, S., and Zuber, A.: Multimodel estimates of intercontinental source-receptor relationships for ozone pollution, *J. Geophys. Res.-Atmos.*, 114, D04301, doi:10.1029/2008JD010816, 2009.
- 770 Fiore, A. M., Mickley, L. J., Zhu, Q. and Baublitz, C. B.: Climate and Tropospheric Oxidizing Capacity, *Annu. Rev. Earth Planet. Sci.*, 52, 11.1–11.29, <https://doi.org/10.1146/annurev-earth-032320-090307>, 2024.
- Gaubert, B., Emmons, L. K., Raeder, K., Tilmes, S., Miyazaki, K., Arellano Jr., A. F., Elguindi, N., Granier, C., Tang, W., Barré, J., Worden, H. M., Buchholz, R. R., Edwards, D. P., Franke, P., Anderson, J. L., Saunio, M., Schroeder, J., Woo, J.-H., Simpson, I. J., Blake, D. R., Meinardi, S., Wennberg, P. O., Crouse, J., Teng, A., Kim, M., Dickerson, R. R., He, H., Ren, X., Pusede, S. E., and Diskin, G. S.: Correcting model biases of CO in East Asia: impact on oxidant distributions during KORUS-AQ, *Atmos. Chem. Phys.*, 20, 14617–14647, <https://doi.org/10.5194/acp-20-14617-2020>, 2020.
- 775 Granier, C., Guether, A., Lamarque, J. F., Mieville, A., Muller, J. F., Olivier, J., Orlando, J., Peters, J., Petron, G., Tyndall, G., and Wallens, S.: POET, a database of surface emissions of ozone precursors, online available at: <http://www.aero.jussieu.fr/projet/ACCENT/POET.php>, 2005.
- 780 Granier, C., S. Darras, H. Denier van der Gon, J. Doubalova, N. Elguindi, B. Galle, M. Gauss, M. Guevara, J.-P. Jalkanen, J. Kuenen, C. Liousse, B. Quack, D. Simpson, K. Sindelarova: The Copernicus Atmosphere Monitoring Service global and regional emissions (April 2019 version), Report April 2019 version, doi:10.24380/d0bn-kx16, 2019
- Griffiths, P. T., Murray, L. T., Zeng, G., Shin, Y. M., Abraham, N. L., Archibald, A. T., Deushi, M., Emmons, L. K., Galbally, I. E., Hassler, B., Horowitz, L. W., Keeble, J., Liu, J., Moeini, O., Naik, V., O'Connor, F. M., Oshima, N., 785 Tarasick, D., Tilmes, S., Turnock, S. T., Wild, O., Young, P. J., and Zanis, P.: Tropospheric ozone in CMIP6 simulations, *Atmos. Chem. Phys.*, 21, 4187–4218, <https://doi.org/10.5194/acp-21-4187-2021>, 2021.
- Ha, P. T. M., Matsuda, R., Kanaya, Y., Taketani, F., and Sudo, K.: Effects of heterogeneous reactions on tropospheric chemistry: a global simulation with the chemistry–climate model CHASER V4.0, *Geosci. Model Dev.*, 14, 3813–3841, <https://doi.org/10.5194/gmd-14-3813-2021>, 2021.
- 790 Heymsfield, A., Winker D., Avery, M., Vaughan, M., Diskin, G., Deng, M., Mitev, V., and Matthey R.: Relationships between Ice Water Content and Volume Extinction Coefficient from In Situ Observations for Temperatures from 0° to –86°C: Implications for Spaceborne Lidar Retrievals, *J. Appl. Meteorol. Clim.*, 53, 479–505, <https://doi.org/10.1175/JAMC-D-13-087.1>, 2014.
- Holmes, C. D., Prather, M. J., Søvde, O. A., and Myhre, G.: Future methane, hydroxyl, and their uncertainties: key climate and emission parameters for future predictions, *Atmos. Chem. Phys.*, 13, 285–302, <https://doi.org/10.5194/acp-13-285-2013>, 2013.
- 795 Holmes, C. D., Bertram, T. H., Confer, K. L., Graham, K. A., Ronan, A. C., Wirks, C. K., & Shah, V.: The role of clouds in the tropospheric NO_x cycle: A new modelling approach for cloud chemistry and its global implications, *Geophys. Res. Lett.*, 46, 4980–4990. <https://doi.org/10.1029/2019GL081990>, 2019.
- 800 Hou, X., Wild, O., Zhu, B., and Lee, J.: Future tropospheric ozone budget and distribution over east Asia under a net-zero scenario, *Atmos. Chem. Phys.*, 23, 15395–15411, <https://doi.org/10.5194/acp-23-15395-2023>, 2023.
- Hou, X., Zhang, Y., Lv, X., Lee, J.: The Impact of Meteorological Conditions and Emissions on Tropospheric Column Ozone Trends in Recent Years. *Remote Sens.*, 15, 5293. <https://doi.org/10.3390/rs15225293>, 2023.
- Jacob, D. J.: Heterogeneous chemistry and tropospheric ozone, *Atmos. Environ.*, 34(12-14), 2131-2159, 2000.
- 805 Jiang, Z., Zhu, R., Miyazaki, K., McDonald, B. C., Klimont, Z., Zheng, B., Boersma, K. F., Zhang, Q., Worden, H., Worden, J. R., Henze, D. K., Jones, D. B. A., van der Gon, H. A. C. D., and Eskes, H.: Decadal variabilities in



- tropospheric nitrogen oxides over United States, Europe, and China, *J. Geophys. Res.-Atmos.*, 127, e2021JD035872, <https://doi.org/10.1029/2021JD035872>, 2022.
- Kendall, M. G.: Rank Correlation Methods, 4th edn., Charles Griffin, London, 1975.
- 810 Lawrence, M. G., Jöckel, P., and von Kuhlmann, R.: What does the global mean OH concentration tell us?, *Atmos. Chem. Phys.*, 1, 37–49, <https://doi.org/10.5194/acp-1-37-2001>, 2001.
- Lelieveld, J., Gromov, S., Pozzer, A., and Taraborrelli, D.: Global tropospheric hydroxyl distribution, budget and reactivity, *Atmos. Chem. Phys.*, 16, 12477–12493, <https://doi.org/10.5194/acp-16-12477-2016>, 2016.
- Liu, J., Strode, S. A., Liang, Q., Oman, L. D., Colarco, P. R., Fleming, E. L., Manyin, M. E., Douglass, A. R., Ziemke, J.
815 R., Lamsal, L. N., Li, C.: Change in tropospheric ozone in the recent decades and its contribution to global total ozone, *J. Geophys. Res.*, 127, e2022JD037170, <https://doi.org/10.1029/2022JD037170>, 2022.
- Logan, J. A., Prather, M. J., Wofsy, S. C., and McElroy, M. B.: Tropospheric chemistry: A global perspective, *J. Geophys. Res.*, 86(C8), 7210–7254, <https://doi.org/10.1029/JC086iC08p07210>, 1981.
- Macintyre, H. L. and Evans, M. J.: Sensitivity of a global model to the uptake of N₂O₅ by tropospheric aerosol, *Atmos. Chem. Phys.*, 10, 7409–7414, <https://doi.org/10.5194/acp-10-7409-2010>, 2010.
820
- Mann, H. B.: Nonparametric tests against trend, *Econometrica*, 13, 245–259, <https://doi.org/10.2307/1907187>, 1945.
- Meinshausen, M., Vogel, E., Nauels, A., Lorbacher, K., Meinshausen, N., Etheridge, D. M., Fraser, P. J., Montzka, S. A., Rayner, P. J., Trudinger, C. M., Krummel, P. B., Beyerle, U., Canadell, J. G., Daniel, J. S., Enting, I. G., Law, R. M., Lunder, C. R., O'Doherty, S., Prinn, R. G., Reimann, S., Rubino, M., Velders, G. J. M., Vollmer, M. K., Wang, R. H. J.,
825 and Weiss, R.: Historical greenhouse gas concentrations for climate modelling (CMIP6), *Geosci. Model Dev.*, 10, 2057–2116, <https://doi.org/10.5194/gmd-10-2057-2017>, 2017.
- Millet, D. B., Guenther, A., Siegel, D. A., Nelson, N. B., Singh, H. B., de Gouw, J. A., Warneke, C., Williams, J., Eerdeken, G., Sinha, V., Karl, T., Flocke, F., Apel, E., Riemer, D. D., Palmer, P. I., and Barkley, M.: Global atmospheric budget of acetaldehyde: 3-D model analysis and constraints from in-situ and satellite observations, *Atmos. Chem. Phys.*, 10, 3405–3425, <https://doi.org/10.5194/acp-10-3405-2010>, 2010.
830
- Miyazaki, K., Eskes, H., Sudo, K., Boersma, K. F., Bowman, K., and Kanaya, Y.: Decadal changes in global surface NO_x emissions from multi-constituent satellite data assimilation, *Atmos. Chem. Phys.*, 17, 807–837, <https://doi.org/10.5194/acp-17-807-2017>, 2017.
- Monks, S. A., Arnold, S. R., Hollaway, M. J., Pope, R. J., Wilson, C., Feng, W., Emmerson, K. M., Kerridge, B. J.,
835 Latter, B. L., Miles, G. M., Siddans, R., and Chipperfield, M. P.: The TOMCAT global chemical transport model v1.6: description of chemical mechanism and model evaluation, *Geosci. Model Dev.*, 10, 3025–3057, <https://doi.org/10.5194/gmd-10-3025-2017>, 2017.
- Montzka, S. A., Krol, M., Dlugokencky, E., Hall, B., Jöckel, P., Lelieveld, J.: Small interannual variability of global atmospheric hydroxyl, *Science*, 331, 67–69, <https://doi.org/10.1126/science.1197640>, 2011.
- 840 Naik, V., Voulgarakis, A., Fiore, A. M., Horowitz, L. W., Lamarque, J.-F., Lin, M., Prather, M. J., Young, P. J., Bergmann, D., Cameron-Smith, P. J., Cionni, I., Collins, W. J., Dalsøren, S. B., Doherty, R., Eyring, V., Faluvegi, G., Folberth, G. A., Josse, B., Lee, Y. H., MacKenzie, I. A., Nagashima, T., van Noije, T. P. C., Plummer, D. A., Righi, M., Rumbold, S. T., Skeie, R., Shindell, D. T., Stevenson, D. S., Strode, S., Sudo, K., Szopa, S., and Zeng, G.: Preindustrial to present-day changes in tropospheric hydroxyl radical and methane lifetime from the Atmospheric Chemistry and
845 Climate Model Intercomparison Project (ACCMIP), *Atmos. Chem. Phys.*, 13, 5277–5298, <https://doi.org/10.5194/acp-13-5277-2013>, 2013.
- Naus, S., Montzka, S. A., Pandey, S., Basu, S., Dlugokencky, E. J., and Krol, M.: Constraints and biases in a



- tropospheric two-box model of OH, *Atmos. Chem. Phys.*, 19, 407–424, <https://doi.org/10.5194/acp-19-407-2019>, 2019.
- 850 Newsome, B. and Evans, M.: Impact of uncertainties in inorganic chemical rate constants on tropospheric composition and ozone radiative forcing, *Atmos. Chem. Phys.*, 17, 14333–14352, <https://doi.org/10.5194/acp-17-14333-2017>, 2017.
- Nicely, J. M., Canty, T. P., Manyin, M., Oman, L. D., Salawitch, R. J., Steenrod, S. D., Strahan, S. E., and Strode, S. A.: Changes in Global Tropospheric OH Expected as a Result of Climate Change Over the Last Several Decades, *J. Geophys. Res.-Atmos.*, 123, 10774–10795, <https://doi.org/10.1029/2018jd028388>, 2018.
- 855 Nicely, J. M., Duncan, B. N., Hanisco, T. F., Wolfe, G. M., Salawitch, R. J., Deushi, M., Haslerud, A. S., Jöckel, P., Josse, B., Kinnison, D. E., Klekociuk, A., Manyin, M. E., Marécal, V., Morgenstern, O., Murray, L. T., Myhre, G., Oman, L. D., Pitari, G., Pozzer, A., Quaglia, I., Revell, L. E., Rozanov, E., Stenke, A., Stone, K., Strahan, S., Tilmes, S., Tost, H., Westervelt, D. M., and Zeng, G.: A machine learning examination of hydroxyl radical differences among model simulations for CCMI-1, *Atmos. Chem. Phys.*, 20, 1341–1361, <https://doi.org/10.5194/acp-20-1341-2020>, 2020.
- 860 Nicely, J. M., Salawitch, R. J., Canty, T., Anderson, D. C., Arnold, S. R., Chipperfield, M. P., Emmons, L. K., Fleming, J., Huijnen, V., Kinnison, D. E., Lamarque, J.-F., Mao, J., Monks, S. A., Steenrod, S. D., Tilmes, S., and Turquety, S.: Quantifying the causes of differences in tropospheric OH within global models, *J. Geophys. Res.-Atmos.*, 122, 1983–2007, <https://doi.org/10.1002/2016JD026239>, 2017.
- Patra, P. K., Krol, M. C., Montzka, S. A., Arnold, T., Atlas, E. L., Lintner, B. R., Stephens, B. B., Xiang, B., Elkins, J. W., Fraser, P. J., Ghosh, A., Hints, E. J., Hurst, D. F., Ishijima, K., Krummel, P. B., Miller, B. R., Miyazaki, K., Moore, 865 F. L., Mühle, J., O'Doherty, S., Prinn, R. G., Steele, L. P., Takigawa, M., Wang, H. J., Weiss, R. F., Wofsy, S. C., Young, D.: Observational evidence for interhemispheric hydroxyl-radical parity, *Nature*, 513, 219–223, <https://doi.org/10.1038/nature13721>, 2014.
- Patra, P. K., Krol, M. C., Prinn, R. G., Takigawa, M., Mühle, J., Montzka, S. A., Lal, S., Yamashita, Y., Naus, S., Chandra, N., Weiss, R. F., Krummel, P. B., Fraser, P. J., O'Doherty, S., and Elkins, J. W.: Methyl Chloroform Continues 870 to Constrain the Hydroxyl (OH) Variability in the Troposphere, *J. Geophys. Res.-Atmos.*, 126, e2020JD033862, <https://doi.org/10.1029/2020JD033862>, 2021.
- Phillips, D. P., Hopkins, F. E., Bell, T. G., Liss, P. S., Nightingale, P. D., Reeves, C. E., Wohl, C., and Yang, M.: Air–sea exchange of acetone, acetaldehyde, DMS and isoprene at a UK coastal site, *Atmos. Chem. Phys.*, 21, 10111–10132, <https://doi.org/10.5194/acp-21-10111-2021>, 2021.
- 875 Pimlott, M. A., Pope, R. J., Kerridge, B. J., Latter, B. G., Knappett, D. S., Heard, D. E., Ventress, L. J., Siddans, R., Feng, W., and Chipperfield, M. P.: Investigating the global OH radical distribution using steady-state approximations and satellite data, *Atmos. Chem. Phys.*, 22, 10467–10488, <https://doi.org/10.5194/acp-22-10467-2022>, 2022.
- Prather, M. J., Holmes, C. D. and Hsu J.: Reactive greenhouse gas scenarios: Systematic exploration of uncertainties and the role of atmospheric chemistry, *Geophys. Res. Lett.*, 39, L09803, <https://doi.org/10.1029/2012GL051440>, 2012.
- 880 Prather, M. J. and Zhu, L.: Resetting tropospheric OH and CH₄ lifetime with ultraviolet H₂O absorption, *Science*, 385, 201–204, <https://doi.org/10.1126/science.adn0415>, 2024.
- Prinn, R. G., Huang, J., Weiss, R. F., Cunnold, D. M., Fraser, P. J., Simmonds, P. G., McCulloch, A., Harth, C., Reimann, S., Salameh, P., O'Doherty, S., Wang, R. H. J., Porter, L. W., Miller, B. R. and Krummel, P. B.: Evidence for variability of atmospheric hydroxyl radicals over the past quarter century, *Geophys. Res. Lett.*, 07809, 885 <https://doi.org/10.1029/2004GL022228>, 2005.
- Prinn, R. G., Weiss, R. F., Fraser, P. J., Simmonds, P. G., Cunnold, D. M., Alyea, F. N., O'Doherty, S., Salameh, P., Miller, B. R., Huang, J., Wang, R. H. J., Hartley, D. E., Harth, C., Steele, L. P., Sturrock, G., Midgley, P. M., McCulloch, A.: A history of chemically and radiatively important gases in air deduced from ALE/GAGE/AGAGE, *J. Geophys. Res.*, 105, 17751–17792, <https://doi.org/10.1029/2000JD900141>, 2000.



- 890 Read, K. A., Carpenter, L. J., Arnold, S. R., Beale, R., Nightingale, P. D., Hopkins, J. R., Lewis, A. C., Lee, J. D., Mendes, L., and Pickering, S. J.: Multiannual observations of acetone, methanol, and acetaldehyde in remote Tropical Atlantic air: Implications for atmospheric OVOC budgets and oxidative capacity, *Environ. Sci. Technol.*, 46, 11028–11039, <https://doi.org/10.1021/es302082p>, 2012.
- Richter, A., Eyring, V., Burrows, J. P., Bovensmann, H., Lauer, A., Sierk, B., & Crutzen, P. J.: Satellite measurements of NO₂ from international shipping emissions, *Geophys. Res. Lett.*, 31(23), L23110. <https://doi.org/10.1029/2004gl020822>, 2004.
- Rolletter, M., Hofzumahaus, A., Novelli, A., Wahner, A., and Fuchs, H.: Kinetics of the reactions of OH with CO, NO, and NO₂ and of HO₂ with NO₂ in air at 1 atm pressure, room temperature, and tropospheric water vapour concentrations, *Atmos. Chem. Phys.*, 25, 3481–3502, <https://doi.org/10.5194/acp-25-3481-2025>, 2025.
- 900 Sen, P. K.: Estimates of the regression coefficient based on Kendall's tau, *J. Am. Stat. Assoc.*, 63, 1379–1389, <https://doi.org/10.1080/01621459.1968.10480934>, 1968.
- Shindell, D. T., Faluvegi, G., Stevenson, D. S., Krol, M. C., Emmons, L. K., Lamarque, J.-F., Pétron, G., Dentener, F. J., Ellingsen, K., Schultz, M. G., Wild, O., Amann, M., Atherton, C. S., Bergmann, D. J., Bey, I., Butler, T., Cofala, J., Collins, W. J., Derwent, R. G., Doherty, R. M., Drevet, J., Eskes, H. J., Fiore, A. M., Gauss, M., Hauglustaine, D. A., Horowitz, L. W., Isaksen, I. S. A., Lawrence, M. G., Montanaro, V., Müller, J.-F., Pitari, G., Prather, M. J., Pyle, J. A., Rast, S., Rodriguez, J. M., Sanderson, M. G., Savage, N. H., Strahan, S. E., Sudo, K., Szopa, S., Unger, N., van Noije, T. P. C., and Zeng, G.: Multimodel simulations of carbon monoxide: Comparison with observations and projected near-future changes, *J. Geophys. Res.*, 111, D19306, <https://doi.org/10.1029/2006JD007100>, 2006.
- Schultz, M. G., Schröder, S., Lyapina, O., Cooper, O. R., Galbally, I., Petropavlovskikh, I., von Schneidmesser, E., Tanimoto, H., Elshorbany, Y., Naja, M., Seguel, R. J., Dauert, U., Eckhardt, P., Feigenspahn, S., Fiebig, M., Hjellbrekke, A.-G., Hong, Y.-D., Kjeld, P. C., Koide, H., Lear, G., Tarasick, D., Ueno, M., Wallasch, M., Baumgardner, D., Chuang, M.-T., Gillett, R., Lee, M., Molloy, S., Moolla, R., Wang, T., Sharps, K., Adame, J. A., Ancellet, G., Apadula, F., Artaxo, P., Barlasina, M. E., Bogucka, M., Bonasoni, P., Chang, L., Colomb, A., Cuevas-Agulló, E., Cupeiro, M., Degórska, A., Ding, A., Fröhlich, M., Frolova, M., Gadhavi, H., Gheusi, F., Gilge, S., Gonzalez, M. Y., Gros, V., Hamad, S. H., Helmig, D., Henriques, D., Hermansen, O., Holla, R., Huber, J., Im, U., Jaffe, D. A., Komala, N., Kubistin, D., Lam, K.-S., Laurila, T., Lee, H., Levy, I., Mazzoleni, C., Mazzoleni, L. R., McClure-Begley, A., Mohamad, M., Murovec, M., Navarro-Comas, M., Nicodim, F., Parrish, D., Read, K. A., Reid, N., Ries, L., Saxena, P., Schwab, J. J., Scorgie, Y., Senik, I., Simmonds, P., Sinha, V., Skorokhod, A. I., Spain, G., Spangl, W., Spoor, R., Springston, S. R., Steer, K., Steinbacher, M., Suharguniyawan, E., Torre, P., Trickl, T., Weili, L., Weller, R., Xu, X., Xue, L., and Ma, Z.: The Tropospheric Ozone Assessment Report: database and metrics data of global surface ozone observations, *Elementa: Science of the Anthropocene*, 5, 58, <https://doi.org/10.1525/elementa.244>, 2017.
- 920 Simpson, D. and Darras, S.: Global soil NO emissions for Atmospheric Chemical Transport Modelling: CAMS-GLOB-SOIL v2.2, *Earth Syst. Sci. Data Discuss.* <https://doi.org/10.5194/essd-2021-221>, 2021.
- Sindelarova, K., Markova, J., Simpson, D., Huszar, P., Karlicky, J., Darras, S., and Granier, C.: High-resolution biogenic global emission inventory for the time period 2000–2019 for air quality modelling, *Earth Syst. Sci. Data*, 14, 251–270, <https://doi.org/10.5194/essd-14-251-2022>, 2022.
- Soulie, A., Granier, C., Darras, S., Zilbermann, N., Doumbia, T., Guevara, M., Jalkanen, J.-P., Keita, S., Liousse, C., Crippa, M., Guizzardi, D., Hoesly, R., and Smith, S. J.: Global anthropogenic emissions (CAMSGLOBANT) for the Copernicus Atmosphere Monitoring Service simulations of air quality forecasts and reanalyses, *Earth Syst. Sci. Data*, 16, 2261–2279, <https://doi.org/10.5194/essd-16-2261-2024>, 2024.
- 930 Spivakovsky, C. M., Logan, J.A., Montzka, S.A., Balkanski, Y., Foreman-Fowler, M.S., Jones, D.B., Horowitz, L.W., Fusco, A.C., Brenninkmeijer, C.A., Prather, M.J., Wofsy, S.C., & McElroy, M.B.: Three-dimensional climatological



- distribution of tropospheric OH: Update and evaluation, *J. Geophys. Res.*, 105, 8931–8980, 2000.
- 935 Stevenson, D. S., Zhao, A., Naik, V., O'Connor, F. M., Tilmes, S., Zeng, G., Murray, L. T., Collins, W. J., Griffiths, P. T., Shim, S., Horowitz, L. W., Sentman, L. T., and Emmons, L.: Trends in global tropospheric hydroxyl radical and methane lifetime since 1850 from AerChemMIP, *Atmos. Chem. Phys.*, 20, 12905–12920, <https://doi.org/10.5194/acp-20-12905-2020>, 2020.
- Stewart, D. J., Griffiths, P. T., and Cox, R. A.: Reactive uptake coefficients for heterogeneous reaction of N₂O₅ with submicron aerosols of NaCl and natural sea salt, *Atmos. Chem. Phys.*, 4, 1381–1388, <https://doi.org/10.5194/acp-4-1381-2004>, 2004.
- 940 Stone, D., Whalley, L. K., Heard, D. E.: Tropospheric OH and HO₂ radicals: Field measurements and model comparisons, *Chem. Soc. Rev.*, 41, 6348–6404, <https://doi.org/10.1039/c2cs35140d>, 2012.
- Strode, S. A., Liu, J., Lait, L., Commane, R., Daube, B., Wofsy, S., Conaty, A., Newman, P., and Prather, M.: Forecasting carbon monoxide on a global scale for the ATom-1 aircraft mission: insights from airborne and satellite observations and modeling, *Atmos. Chem. Phys.*, 18, 10955–10971, <https://doi.org/10.5194/acp-18-10955-2018>, 2018.
- 945 Tabazadeh, A., Yokelson, R. J., Singh, H. B., Hobbs, P. V., Crawford, J. H., and Iraci, L. T.: Heterogeneous chemistry involving methanol in tropospheric clouds, *Geophys. Res. Lett.*, 31, L06114, doi:10.1029/2003GL018775, 2004.
- Talukdar, R. K., Longfellow, C. A., Gilles, M. K., and Ravishankara, A. R.: Quantum yields of O(¹D) in the photolysis of ozone between 289 and 329 nm as a function of temperature, *Geophys. Res. Lett.*, 25, 143–146, <https://doi.org/10.1029/97GL03354>, 1998.
- 950 Tan, D., Faloon, I., Simpas, J. B., Brune, W., Olson, J., Crawford, J., Avery, M., Sachse, G., Vay, S., Sandholm, S., Guan, H.-W., Vaughn, T., Mastromarino, J., Heikes, B., Snow, J., Podolske, J., and Singh, H.: OH and HO₂ in the tropical Pacific: Results from PEM-Tropics B, *J. Geophys. Res.-Atmos.*, 106, 32667–32681, <https://doi.org/10.1029/2001JD900002>, 2001.
- 955 Theil, H.: A rank-invariant method of linear and polynomial regression analysis, *Proc. Kon. Ned. Akad. Wetensch.*, 53, 386–392, https://link.springer.com/chapter/10.1007/978-94-011-2546-8_20, 1950.
- Thompson, R. L., Montzka, S. A., Vollmer, M. K., Arduini, J., Crotwell, M., Krummel, P. B., Lunder, C., Mühle, J., O'Doherty, S., Prinn, R. G., Reimann, S., Vimont, I., Wang, H., Weiss, R. F., and Young, D.: Estimation of the atmospheric hydroxyl radical oxidative capacity using multiple hydrofluorocarbons (HFCs), *Atmos. Chem. Phys.*, 24, 1415–1427, <https://doi.org/10.5194/acp-24-1415-2024>, 2024.
- 960 Thompson, C. R., Wofsy, S. C., Prather, M. J., Newman, P. A., Hanisco, T. F., Ryerson, T. B., Fahey, D. W., Apel, E. C., Brock, C. A., Brune, W. H., Froyd, K., Katich, J. M., Nicely, J. M., Peischl, J., Ray, E., Veres, P. R., Wang, S., Allen, H. M., Asher, E., Bian, H., Blake, D., Bourgeois, I., Budney, J., Bui, T. P., Butler, A., Campuzano-Jost, P., Chang, C., Chin, M., Commane, R., Correa, G., Crouse, J. D., Daube, B., Dibb, J. E., DiGangi, J. P., Diskin, G. S., Döllner, M., Elkins, J. W., Fiore, A. M., Flynn, C. M., Guo, H., Hall, S. R., Hannun, R. A., Hills, A., Hints, E. J., Hodzic, A., Hornbrook, R. S., Huey, L. G., Jiménez-Palacios, J. L., Keeling, R. F., Kim, M. J., Kupe, A., Lacey, F., Lait, L. R., Lamarque, J.-F., Liu, J., McKain, K., Meinardi, S., Miller, D. O., Montzka, S. A., Moore, F. L., Morgan, E. J., Murphy, D. M., Murray, L. T., Nault, B. A., Neuman, J. A., Nguyen, L., Gonzalez, Y., Rollins, A., Rosenlof, K., Sargent, M., Schill, G., Schwarz, J. P., St. Clair, J. M., Steenrod, S. D., Stephens, B. B., Strahan, S. E., Strode, S. A., Sweeney, C., Thames, A. B., Ullmann, K.,
- 970 Wagner, N., Weber, R., Weinzierl, B., Wennberg, P. O., Williamson, C. J., Wolfe, G. M., Zeng, L.: The NASA Atmospheric Tomography (ATom) Mission: Imaging the Chemistry of the Global Atmosphere, *Bull. Am. Meteorol. Soc.*, 103 (3), E761–E790, <https://doi.org/10.1175/BAMS-D-20-0315.1>, 2022.
- Thornton, J. A., Braban, C. F. and Abbatt, J. P. D.: N₂O₅ hydrolysis on sub-micron organic aerosols: The effect of relative humidity, particle phase, and particle size, *Phys. Chem. Chem. Phys.*, 5(20), 4593–4603,



- 975 <https://doi.org/10.1039/B307498F>, 2003.
- Tie, X., Emmons, L., Horowitz, L., Brasseur, G., Ridley, B., Atlas, E., Hess, P., Klonecki, A., Madronich, S., Talbot, R., Dibb, J., Marbouty, D., and Hennessy, J.: Effect of sulfate aerosol on tropospheric NO_x and ozone budgets model simulations and TOPSE evidence, *J. Geophys. Res.*, 108(D4), 8364, <https://doi.org/10.1029/2001JD001508>, 2003.
- Travis, K. R., Heald, C. L., Allen, H. M., Apel, E. C., Arnold, S. R., Blake, D. R., Brune, W. H., Chen, X., Commane, R., Crouse, J. D., Daube, B. C., Diskin, G. S., Elkins, J. W., Evans, M. J., Hall, S. R., Hints, E. J., Hornbrook, R. S., Kasibhatla, P. S., Kim, M. J., Luo, G., McKain, K., Millet, D. B., Moore, F. L., Peischl, J., Ryerson, T. B., Sherwen, T., Thames, A. B., Ullmann, K., Wang, X., Wennberg, P. O., Wolfe, G. M., and Yu, F.: Constraining remote oxidation capacity with ATom observations, *Atmos. Chem. Phys.*, 20, 7753–7781, <https://doi.org/10.5194/acp-20-7753-2020>, 2020.
- 980
- Turner, A. J., Frankenberg, C., and Kort, E. A.: Interpreting contemporary trends in atmospheric methane, *P. Natl. Acad. Sci.*, 116, 2805–2813, <https://doi.org/10.1073/pnas.1814297116>, 2019.
- 985
- Turner, A. J., Frankenberg, C., Wennberg, P. O., Jacob, D. J.: Ambiguity in the causes for decadal trends in atmospheric methane and hydroxyl, *P. Natl. Acad. Sci.*, 114, 5367–5372, <https://doi.org/10.1073/pnas.1616020114>, 2017.
- van der Werf, G. R., Randerson, J. T., Giglio, L., van Leeuwen, T. T., Chen, Y., Rogers, B. M., Mu, M., van Marle, M. J. E., Morton, D. C., Collatz, G. J., Yokelson, R. J., and Kasibhatla, P. S.: Global fire emissions estimates during 1997–2016, *Earth Syst. Sci. Data*, 9, 697–720, <https://doi.org/10.5194/essd-9-697-2017>, 2017.
- 990
- Wang, H., Lu, X., Jacob, D. J., Cooper, O. R., Chang, K.-L., Li, K., Gao, M., Liu, Y., Sheng, B., Wu, K., Wu, T., Zhang, J., Sauvage, B., Nédélec, P., Blot, R., and Fan, S.: Global tropospheric ozone trends, attributions, and radiative impacts in 1995–2017: an integrated analysis using aircraft (IAGOS) observations, ozonesonde, and multi-decadal chemical model simulations, *Atmos. Chem. Phys.*, 22, 13753–13782, <https://doi.org/10.5194/acp-22-13753-2022>, 2022.
- 995
- Wang, S., Hornbrook, R. S., Hills, A., Emmons, L. K., Tilmes, S., Lamarque, J.-F., et al. Atmospheric acetaldehyde: Importance of air-sea exchange and a missing source in the remote troposphere. *Geophys. Res. Lett.*, 46, 5601–5613. <https://doi.org/10.1029/2019GL082034>, 2019.
- Wild, O.: Modelling the global tropospheric ozone budget: exploring the variability in current models, *Atmos. Chem. Phys.*, 7, 2643–2660, <https://doi.org/10.5194/acp-7-2643-2007>, 2007.
- 1000
- Wild, O. and Prather, M. J.: Excitation of the primary tropospheric chemical mode in a global 3-D model, *J. Geophys. Res.*, 105, 24 647–24 660, 2000.
- Wild, O., Voulgarakis, A., O’Connor, F., Lamarque, J.-F., Ryan, E. M., and Lee, L.: Global sensitivity analysis of chemistry–climate model budgets of tropospheric ozone and OH: exploring model diversity, *Atmos. Chem. Phys.*, 20, 4047–4058, <https://doi.org/10.5194/acp-20-4047-2020>, 2020.
- 1005
- Wofsy, S., Afshar, S., Allen, H., Apel, E., Asher, E., Barletta, B., Bent, J., Bian, H., Biggs, B., Blake, D., Blake, N., Bourgeois, I., Brock, C., Brune, W., Budney, J., Bui, T., Butler, A., Campuzano-Jost, P., Chang, C., Chin, M., Commane, R., Correa, G., Crouse, J., Cullis, P., Daube, B., Day, D., Dean-Day, J., Dibb, J., DiGangi, J., Diskin, G., Dollner, M., Elkins, J., Erdesz, F., Fiore, A., Flynn, C., Froyd, K., Gesler, D., Hall, S., Hanisco, T., Hannun, R., Hills, A., Hints, E., Hoffman, A., Hornbrook, R., Huey, L., Hughes, S., Jimenez, J., Johnson, B., Katich, J., Keeling, R., Kim, M., Kupc, A., Lait, L., McKain, K., Mclaughlin, R., Meinardi, S., Miller, D., Montzka, S., Moore, F., Morgan, E., Murphy, D., Murray, L., Nault, B., Neuman, J., Newman, P., Nicely, J., Pan, X., Paplawsky, W., Peischl, J., Prather, M., Price, D., Ray, E., Reeves, J., Richardson, M., Rollins, A., Rosenlof, K., Ryerson, T., Scheuer, E., Schill, G., Schroder, J., Schwarz, J., St.Clair, J., Steenrod, S., Stephens, B., Strode, S., Sweeney, C., Tanner, D., Teng, A., Thames, A., Thompson, C., Ullmann, K., Veres, P., Wagner, N., Watt, A., Weber, R., Weinzierl, B., Wennberg, P., Williamson, C., Wilson, J., Wolfe, G., Woods, C., Zeng, L., and Vieznor, N.: ATom: Merged Atmospheric Chemistry, Trace Gases, and Aerosols, Version 2
- 1010
- 1015



- (Version 2.0), ORNL Distributed Active Archive Center, <https://doi.org/10.3334/ORNLDAAAC/1925>, 2021.
- 1020 Yang, M., Beale, R., Liss, P., Johnson, M., Blomquist, B., and Nightingale, P.: Air–sea fluxes of oxygenated volatile organic compounds across the Atlantic Ocean, *Atmos. Chem. Phys.*, 14, 7499–7517, <https://doi.org/10.5194/acp-14-7499-2014>, 2014.
- Yin, Y., Chevallier, F., Ciais, P., Broquet, G., Fortems-Cheiney, A., Pison, I., and Saunois, M.: Decadal trends in global CO emissions as seen by MOPITT, *Atmos. Chem. Phys.*, 15, 13433–13451, <https://doi.org/10.5194/acp-15-13433-2015>, 2015.
- 1025 Young, P. J., Naik, V., Fiore, A. M., Gaudel, A., Guo, J., Lin, M. Y., Neu, J. L., Parrish, D. D., Rieder, H. E., Schnell, J. L., Tilmes, S., Wild, O., Zhang, L., Ziemke, J., Brandt, J., Delcloo, A., Doherty, R. M., Geels, C., Hegglin, M. I., Hu, L., Im, U., Kumar, R., Luhar, A., Murray, L., Plummer, D., Rodriguez, J., Saiz-Lopez, A., Schultz, M. G., Woodhouse, M. T., and Zeng, G.: Tropospheric Ozone Assessment Report: Assessment of global-scale model performance for global and regional ozone distributions, variability, and trends, *Elem. Sci. Anthr.*, 6, 10, <https://doi.org/10.1525/elementa.265>, 2018.
- 1030 Zara, M., Boersma, K. F., De Smedt, I., Richter, A., Peters, E., van Geffen, J. H. G. M., Beirle, S., Wagner, T., Van Roozendaal, M., Marchenko, S., Lamsal, L. N., and Eskes, H. J.: Improved slant column density retrieval of nitrogen dioxide and formaldehyde for OMI and GOME-2A from QA4ECV: intercomparison, uncertainty characterisation, and trends, *Atmos. Meas. Tech.*, 11, 4033–4058, <https://doi.org/10.5194/amt-11-4033-2018>, 2018.
- 1035 Zhao, Y., Saunois, M., Bousquet, P., Lin, X., Berchet, A., Hegglin, M. I., Canadell, J. G., Jackson, R. B., Hauglustaine, D. A., Szopa, S., Stavert, A. R., Abraham, N. L., Archibald, A. T., Bekki, S., Deushi, M., Jöckel, P., Josse, B., Kinnison, D., Kirner, O., Maréchal, V., O’Connor, F. M., Plummer, D. A., Revell, L. E., Rozanov, E., Stenke, A., Strode, S., Tilmes, S., Dlugokencky, E. J., and Zheng, B.: Inter-model comparison of global hydroxyl radical (OH) distributions and their impact on atmospheric methane over the 2000–2016 period, *Atmos. Chem. Phys.*, 19, 13701–13723, <https://doi.org/10.5194/acp-19-13701-2019>, 2019.
- 1040 Zhao, Y., Saunois, M., Bousquet, P., Lin, X., Berchet, A., Hegglin, M. I., Canadell, J. G., Jackson, R. B., Deushi, M., Jöckel, P., Kinnison, D., Kirner, O., Strode, S., Tilmes, S., Dlugokencky, E. J., and Zheng, B.: On the role of trend and variability in the hydroxyl radical (OH) in the global methane budget, *Atmos. Chem. Phys.*, 20, 13011–13022, <https://doi.org/10.5194/acp-20-13011-2020>, 2020.
- 1045 Zhao, Y. H., Zheng, B., Saunois, M., Philippe Ciais, P., Michaela I. Hegglin, M. I., Lu, S. M., Li, Y. F., Philippe Bousquet, P.: Air pollution modulates trends and variability of the global methane budget, *Nature*, 642, 369–375, <https://doi.org/10.1038/s41586-025-09004-z>, 2025.
- Zheng, B., Chevallier, F., Ciais, P., Yin, Y., Deeter, M. N., Worden, H. M., Wang, Y., Zhang, Q., and He, K.: Rapid decline in carbon monoxide emissions and export from East Asia between years 2005 and 2016, *Environ. Res. Lett.*, 13, 044007, <https://doi.org/10.1088/1748-9326/aab2b3>, 2018.
- 1050 Ziemke, J. R., Chandra, S., Duncan, B. N., Froidevaux, L., Bhartia, P. K., Levelt, P. F., and Waters, J. W.: Tropospheric ozone determined from Aura OMI and MLS: Evaluation of measurements and comparison with the Global Modeling Initiative’s Chemical Transport Model, *J. Geophys. Res.*, 111, D19303, <https://doi.org/10.1029/2006JD007089>, 2006.
- 1055 Ziemke, J. R., Oman, L. D., Strode, S. A., Douglass, A. R., Olsen, M. A., McPeters, R. D., Bhartia, P. K., Froidevaux, L., Labow, G. J., Witte, J. C., Thompson, A. M., Haffner, D. P., Kramarova, N. A., Frith, S. M., Huang, L.-K., Jaross, G. R., Seftor, C. J., Deland, M. T., and Taylor, S. L.: Trends in global tropospheric ozone inferred from a composite record of TOMS/OMI/MLS/OMPS satellite measurements and the MERRA-2 GMI simulation, *Atmos. Chem. Phys.*, 19, 3257–3269, <https://doi.org/10.5194/acp-19-3257-2019>, 2019.